

Dynamical Expansion of Ionization and Dissociation Front around a Massive Star. II. On the Generality of Triggered Star Formation

Takashi Hosokawa¹ and Shu-ichiro Inutsuka²

ABSTRACT

We analyze the dynamical expansion of the H II region, photodissociation region, and the swept-up shell, solving the UV- and FUV-radiative transfer, the thermal and chemical processes in the time-dependent hydrodynamics code. Following our previous paper, we investigate the time evolutions with various ambient number densities and central stars. Our calculations show that basic evolution is qualitatively similar among our models with different parameters. The molecular gas is finally accumulated in the shell, and the gravitational fragmentation of the shell is generally expected. The quantitative differences among models are well understood with analytic scaling relations. The detailed physical and chemical structure of the shell is mainly determined by the incident FUV flux and the column density of the shell, which also follow the scaling relations. The time of shell-fragmentation, and the mass of the gathered molecular gas are sensitive to the ambient number density. In the case of a low density, the shell-fragmentation occurs over a longer timescale, and the accumulated molecular gas is more massive than in the case of a high density. The variations with different central stars are more moderate. The time of the shell-fragmentation differs by a factor of several with the various stars of $M_* = 12 - 101 M_\odot$. According to our numerical results, we conclude that the expanding H II region should be an efficient trigger for star formation in molecular clouds if the mass of the ambient molecular material is large enough.

Subject headings: Circumstellar matter – H II regions – ISM: molecules – STARS : formation

¹Division of Theoretical Astrophysics, National Astronomical Observatory, Mitaka, Tokyo 181-8588, Japan ; hosokawa@th.nao.kyoto-u.ac.jp

²Department of Physics, Kyoto University, Kyoto 606-8502 ; inutsuka@tap.sephys.kyoto-u.ac.jp

1. Introduction

Massive stars are ubiquitous in many star-forming regions, and their feedback processes have significant impacts on the surrounding interstellar medium (ISM). UV/FUV radiation photoionizes/photodissociates molecular gas, and the H II and photodissociation regions (PDR) expand around the massive star. The stellar winds and supernovae explosions give rise to expanding bubbles in ISM. The role of these feedback processes in relation to ISM has been studied from two competing perspectives on their effects on star-formation activity. The expanding H II region and bubble erode the parental molecular clouds and suppress star formation (*negative feedback*). On the other hand, the shock front (SF) emerges as the high-pressure region expands. The SF compresses the ISM and star formation can be triggered in very dense layers (*positive feedback*).

In this paper, we focus on the H II regions and their feedback processes. The role of the expanding H II regions is also discussed in terms of negative and positive feedback processes. Most of the massive stars are born in the giant molecular clouds (GMCs) and H II regions begin to expand in the dense cores and clumps in GMCs (ultra compact H II regions, e.g., Churchwell 2002). As the H II region expands, the molecular gas is gradually eroded. When the IF reaches the cloud surface, the ionized gas spouts from the cloud (“champagne flow”, see Tenorio-Tagle 1979). The molecular material around massive stars is dispersed, so that star formation is quenched (e.g., Whitworth 1979; Franco et al. 1994). On the other hand, the SF emerges in front of the IF owing to the pressure excess of the H II region. The SF sweeps up the ISM to form a shell and star formation will be induced by the instability of the shell (“collect and collapse” scenario ; see, e.g., Elmegreen & Lada 1977; Elmegreen 1989, and references therein). The SF also compresses pre-existing globules through their photoevaporation and star formation will be triggered (radiative implosion ; see, e.g., Bertoldi 1989; Bertoldi & McKee 1990).

The hydrodynamical expansion of the H II regions has been studied numerically (e.g., Mathews 1965; Tenorio-Tagle 1979; Franco et al. 1990; Garcia-Segura & Franco 1998). These efforts have successfully shown the various dynamical aspects of the expansion in both homogeneous and inhomogeneous ambient media. However, these do not include the outer PDR and thermal processes that should be dominant there. Hill & Hollenbach (1978) have analytically shown that the dissociation fronts (DFs) initially expand outside the SF, but finally slow down to be taken into the shell. Roger & Dewdney (1992) and Diaz-Miller et al. (1998) studied the expansion of the H II region and outer PDR around a single massive star, solving the radiative transfer of UV and FUV photons. Although the hydrodynamics has not been included, they have shown that a significant amount of the molecular gas is not ionized but photodissociated. Diaz-Miller et al. (1998) have pointed out that the photodissociation

of the molecular gas reduces the star-forming capacity of the cloud

Deharveng et al. (2003) have provided a good simple example to investigate the role of the expanding H II region. They have observed the molecular fragments around the galactic H II region, Sharpless 104 (Sh104), and found a young cluster within the core of one fragment. They have argued that this is clear evidence of the “collect and collapse” model. In our previous paper (Hosokawa & Inutsuka 2005, hereafter, Paper I), we have modeled Sh104 performing the hydrodynamical calculation including the PDR and the swept-up shell as well as the H II region. Our calculation has shown that the molecular shell forms around the H II region shielding the FUV radiation. The abundance of the accumulated molecules shows excellent agreement with the observation. We have also suggested a role for the expanding H II regions as a positive feedback process. The swept-up mass remains in the shell and the shell can be dominated by the cold molecular gas shielding UV and FUV photons.

Recently, Deharveng et al. (2005) have reported dozens of galactic H II regions similar to Sh104, which show that such triggering is a common process in some situations. So, the next interesting questions to answer are the following :

- How does the time evolution change with differing ambient number density and mass of the central star? Is the molecular gas always accumulated in the shell? If the evolution change with a different ambient density or central star, why so?

To answer these questions, we investigate the time evolution of the H II region, PDR, and the swept-up shell with various ambient number densities and central stars. As in Paper I, the UV- and FUV-radiative transfer and the thermal and chemical processes are solved using a time-dependent hydrodynamics code. We show the numerical results of some representative models and explain what causes the differences among models. We can show that, in many cases, the FUV photons are shielded and the molecular gas is finally gathered in the shell.

The organization of this paper is as follows: In §2, we explain the input physics of our code. The subsequent §3 is devoted to showing the procedures of the numerical calculation. §4 and 5 are the main part of this paper, where the numerical results are shown. The dependence on the ambient number density, and on the luminosity (mass) of the central star is studied in each section. §6 and 7 are assigned to discussions and conclusions.

2. Input Physics for Calculation

2.1. Basic Equations

2.1.1. Hydrodynamic Equations

In this paper, we consider the spherical expansion of the H II region. The hydrodynamic equations of the system are written as,

$$\frac{d}{dt} \left(\frac{1}{\rho} \right) - \frac{\partial(r^2 u)}{\partial m} = 0, \quad (1)$$

$$\frac{du}{dt} + r^2 \frac{\partial p}{\partial m} = 0, \quad (2)$$

$$\rho \left(\frac{dE}{dt} + \frac{\partial(r^2 u p)}{\partial m} + \frac{\partial(r^2 q_{\text{cond}})}{\partial m} \right) = n(\Gamma - \Lambda), \quad (3)$$

$$p = \{0.5(1 + 3X_{\text{H}^+} + X_{\text{H}}) + Y_{\text{He}}\} nkT, \quad (4)$$

$$\rho = (1 + 4Y_{\text{He}})m_{\text{H}}n \equiv \mu m_{\text{H}}n, \quad (5)$$

where m is the mass coordinate defined as $dm = \rho r^2 dr$, ρ is the mass density, n is the number density of the hydrogen nucleon, u is the velocity, p is the gas pressure, and E is the total energy, including the kinetic energy ($u^2/2$) and the thermal energy ($e \equiv p/(\gamma - 1)/\rho$) per unit mass. We adopt $\gamma = 5/3$ for simplicity. In the above equations, X_{H^+} (X_{H}) is the number ratio defined as n_{H^+}/n (n_{H}/n), and Y_{He} is the abundance of He atoms. In the energy equation, Γ and Λ represent the heating and cooling rates per hydrogen nucleon, and q_{cond} is the heat transfer by thermal conduction. We include 5 heating processes and 12 cooling processes to calculate Γ and Λ (see §2.2). The thermal conduction is needed to satisfy the “Field condition” (see Appendix B). We do not include the self-gravity of the gas to study the simple situation of the HII region expanding into a homogeneous medium. Even if we include the gas self-gravity, the H II region quickly expands at the velocity of $\sim 10 \text{ km/s}$, and the smaller inward velocity caused by the self-gravity does not significantly affect our results. The gravity of the central star does not affect the evolution of H II regions, unless the H II region is very small. The radius where the velocity of escape from the star is comparable to the sound speed of the H II region is $\sim 10^{-3} (M_*/10M_{\odot}) \text{ pc}$, where M_* is the stellar mass. This is much smaller than the initial Strömgen radius,

$$R_{\text{st}} = 0.64 \text{ pc} \left(\frac{S_{\text{UV}}}{10^{49} \text{ s}^{-1}} \right)^{1/3} \left(\frac{T_{\text{HII}}}{10^4 \text{ K}} \right)^{1/4} \left(\frac{n}{10^3 \text{ cm}^{-3}} \right)^{-2/3}, \quad (6)$$

with the number density considered in this paper, $n \leq 10^4 \text{ cm}^{-3}$.

The procedure to calculate a whole set of equations is explained in §3.1.

Table 1. Properties of massive stars with solar metallicity (Diaz-Miller et al. 1998)

T_{eff} (10^4 K) ^a	M_* (M_\odot) ^b	$\log(S_{\text{UV}}(\text{s}^{-1}))^c$	$\log(S_{\text{FUV}}(\text{s}^{-1}))^d$	$\log(S_{\text{FUV}}/S_{\text{UV}})$
5.0	101.3	49.89	49.54	-0.35
4.0	40.9	48.78	48.76	-0.02
3.3	19.0	47.75	48.21	0.54
2.4	11.7	45.38	47.39	2.01

a : effective temperature, b : stellar mass, c, d : emission rates of UV and FUV photons

2.1.2. Radiative Transfer Equations

We solve the radiative transfer of both UV and FUV photons. UV photons photoionize atoms in the H II region and heat up the gas by the photoionization. FUV photons photodissociate molecules in the PDR and heat up the gas mainly by the ionization of the dust grains (photoelectric heating).

We solve the UV ($h\nu > 13.6$ eV) and FUV (11.0 eV $< h\nu < 13.6$ eV) radiative transfer separately to avoid the time-consuming calculation. The UV radiative transfer equation is,

$$\frac{1}{r^2} \frac{\partial(r^2 F_{\nu,\text{UV}})}{\partial r} = -n(1 - X_{\text{H}^+})\sigma_{\nu,\text{UV}}F_{\nu,\text{UV}}, \quad (7)$$

where $F_{\nu,\text{UV}} d\nu$ is the UV photon number flux at the frequency range, $\nu \rightarrow \nu + d\nu$ and $\sigma_{\nu,\text{UV}}$ is the cross section for the photoionization of hydrogen atoms. Equation (7) is solved as

$$F_{\nu,\text{UV}} = \frac{S_{\nu,\text{UV}}}{4\pi r^2} \exp(-\tau_{\nu,\text{UV}}), \quad (8)$$

where $S_{\nu,\text{UV}} d\nu$ is the photon number luminosity from the central star at a frequency range of $\nu \rightarrow \nu + d\nu$, and $\tau_{\nu,\text{UV}}$ is the opacity written as,

$$\tau_{\nu,\text{UV}} = \int n(1 - X_{\text{H}^+})\sigma_{\nu,\text{UV}} dr. \quad (9)$$

Diaz-Miller et al. (1998) provide the frequency-integrated photon number luminosities of massive stars in UV and FUV range. They have calculated with the line-bracketed LTE atmosphere models by Kurucz (1993). We use their results for the solar metallicity listed in Table 1. Note that some recent works present slightly larger values of S_{UV} and S_{FUV} . For example, S_{UV} given by Martins, Schaerer & Hiller (2005) is larger by a factor of ~ 1.5 (3.0) for $20 M_\odot$ ($40 M_\odot$) star than the adopted values. We have calculated the ratio, $S_{\text{UV}}/S_{\text{FUV}}$ with the model spectrum distributed by Lanz & Hubeny (2003), and found that S_{FUV} is also larger than the values in Table.1 only by a factor of less than 2. However,

these differences by a factor of a few do not significantly affect our quantitative analysis. We approximate the spectrum of the Lyman-continuum, $S_{\nu,UV}$, by the Planck function of the effective temperature, T_{eff} and normalize $S_{\nu,UV}$ so that the integrated UV luminosity agrees with the values listed in Table 1. We adopt the frequency-dependent cross section,

$$\sigma_{\nu,UV} = 6.3 \times 10^{-18} \left(\frac{\nu}{\nu_{Ly1}} \right)^{-2.8} \text{ (cm}^2\text{)}, \quad (10)$$

where ν_{Ly1} corresponds to the Lyman limit, $h\nu_{Ly1} = 13.6$ eV. We do not take into account the absorption of ionizing photons by dust inside the HII region because of the uncertain size distribution of grains. We discuss the effect of the dust in the H II region in §6.1.1. The diffuse UV radiation produced by the recombination is treated by the on-the-spot approximation.

The treatment of the FUV radiative transfer is a little more complicated. Hydrogen and carbon monoxide molecules are photodissociated by the line absorption of energetic photons ($11 \text{ eV} < h\nu < 13.6 \text{ eV}$). Lower energetic photons ($h\nu < 11 \text{ eV}$) also contribute to some other processes. For example, photons of $h\nu > 6 \text{ eV}$ (typical work function of grains) contribute to the photoelectric heating and the dust recombination cooling (Bakes & Tielens 1994). Below, we solve the transfer of three types of FUV flux separately, which are for the photodissociation of H_2 molecules, CO molecules, and for other microprocesses.

We use the FUV flux, F_{ν,H_2} to calculate the photodissociation rate of hydrogen molecules with the self-shielding effect. The radiative transfer equation for F_{ν,H_2} is,

$$\frac{1}{r^2} \frac{\partial(r^2 F_{\nu,H_2})}{\partial r} = -n(0.5X_{H_2}\sigma_{\nu,H_2} + \sigma_d)F_{\nu,H_2}, \quad (11)$$

where σ_{ν,H_2} and σ_d are the cross section of the photodissociation of hydrogen molecules and the dust absorption, X_{H_2} is the molecular ratio defined as, $X_{H_2} \equiv 2n_{H_2}/n = 1 - X_{H^+} - X_H$. The dust attenuation law for the H_2 photodissociating photons is $\exp(-2.5A_V)$ (Tielens & Hollenbach 1985), and we adopt the corresponding cross section, $\sigma_d = 1.2 \times 10^{-21} \text{ cm}^2$. Equation (11) is solved as,

$$F_{\nu,H_2} = \frac{S_{\nu,H_2}}{4\pi r^2} \exp(-\tau_{\nu,H_2}), \quad (12)$$

where $S_{\nu,H_2} d\nu$ is the FUV photon number luminosity at $\nu \rightarrow \nu + d\nu$ and $\tau_{H_2,\nu}$ is the optical depth given by,

$$\tau_{\nu,H_2} = \int n (0.5X_{H_2}\sigma_{\nu,H_2} + \sigma_d) dr. \quad (13)$$

The photodissociation of H_2 molecules occurs via a so-called ‘‘Solomon process’’ (Stecher & Williams 1967). We assume that all H_2 molecules are at the rotational-vibrational levels of $v = 0, J = 0$ (ortho) or $v = 0, J = 1$ (para) of the ground electronic level. The ortho-to-para ratio is assumed to be a typical value, 3:1, which is the limit for the high

temperature (Hollenbach & Salpeter 1970). We consider only transitions via Lyman-bands, which are the main channels for the “Solomon process”. In the Lyman-band transitions, the rotational quantum number changes as $\Delta J = -1$ (P transition) or $\Delta J = +1$ (R transition). Therefore, only 3 types of transitions are possible for each excited vibrational level in $B^1\Sigma_u^+$, v' ; $(v, J) = (0, 0) \rightarrow (v', 1)$, $(0, 1) \rightarrow (v', 0)$, and $(0, 1) \rightarrow (v', 2)$. The vibrational quantum number, v and v' , can change freely. For the line profile for each transition, we adopt a Voigt profile,

$$\phi_j(\nu) = \frac{\gamma_j}{4\pi^2\Delta\nu_D} \int_{-\infty}^{+\infty} \frac{\exp(-y^2)}{(v-y)^2 + (\gamma_j/4\pi\Delta\nu_D)^2} dy, \quad (14)$$

where γ_j is the natural line width, $\Delta\nu_D$ is the Doppler width, and $v = (\nu - \nu_0)/\Delta\nu_D$, where ν_0 is the frequency of the line center. In our calculation, we use the constant temperature, $T = 100$ K to calculate the Voigt profile. We have confirmed that our numerical results are not sensitive to T or $\Delta\nu_D$. As noted by Hollenbach et al. (1971), the column density of H_2 molecules easily exceeds 10^{19} (cm^{-2}), then the Lorentz wings dominate the absorption of FUV photons rather than Doppler cores (see Fig. 1 below). The frequency-dependent cross section of the line is,

$$\sigma_j(\nu) = \frac{1}{\sqrt{\pi}} \frac{\sigma_j}{\Delta\nu_D} \phi_j(\nu). \quad (15)$$

The total cross section, σ_j is given by $\sigma_j = \pi e^2/m_e c \cdot f_j$, where f_j is the oscillator strength. Numerical values of f_j , γ_j , and ν_0 are taken from Allison & Dalgarno (1970), Abgrall et al. (1992), and Abgrall et al. (1993). Although there are about 20 sets of three lines of Lyman-bands in $11.0 \text{ eV} < h\nu < 13.6 \text{ eV}$, we approximate these many lines by adopting a representative set of lines. We pick up three $v' = 12$ lines. The logarithmic grids are set around these lines ($12.82 \text{ eV} < h\nu < 12.93 \text{ eV}$) so that the resolution becomes higher around each line center. We consider the constant radiation field, S_{ν, H_2} in this frequency range and normalize this so that the integrated luminosity is equal to the value listed in Table 1. The absorption cross section for Lyman-bands is calculated taking into account the line overlap,

$$\sigma_{\nu, H_2} = (1 - f_{\text{rem}}) \sum_j h_j \sigma_j(\nu), \quad (16)$$

(see Fig. 1) where h_j is the ratio of ortho or para H_2 molecules and f_{rem} is the probability of the reemission. We adopt $f_{\text{rem}} = 0.14$ following Shull (1978). About another 15% of the pumped H_2 molecules decay to be dissociated (see §2.1.3). We assume that the other pumped molecules decay to the excited (v, J) levels in the ground electronic state, followed by an infrared cascade. Fig. 1 shows the absorption cross section of the hydrogen molecules, σ_{ν, H_2} and the dust grains for which we adopted σ_d . As this figure shows, the effect of line overlap of Lyman-bands works at the column density, $N_{H_2} \geq 10^{20} \text{ cm}^{-2}$. About half of FUV

photons are absorbed by dust grains rather than H₂ molecules, because σ_d is larger than σ_{ν, H_2} in the feet of the Lorentz wings.

The photodissociation of CO molecules is also caused by the line absorption of FUV photons (van Dishoeck & Black 1988). Since the distribution of such lines and the line overlapping with Lyman-Werner bands are complicated, we use other FUV flux, $F_{\nu, \text{CO}}$ to calculate the CO photodissociation rate with some shielding effects in the minimal frequency range. The radiative transfer equation for $F_{\nu, \text{CO}}$ is,

$$\frac{1}{r^2} \frac{\partial(r^2 F_{\nu, \text{CO}})}{\partial r} = -n(X_{\text{CO}} Z_C \sigma_{\nu, \text{CO}} + 0.5 X_{\text{H}_2} \sigma_{\text{H}_2, \text{CO}} + \sigma_{d, \text{CO}}) F_{\nu, \text{CO}}, \quad (17)$$

where X_{CO} is the molecular fraction defined as, $X_{\text{CO}} \equiv n_{\text{CO}}/(Z_C n)$, Z_C is the abundance of C atoms, $\sigma_{\nu, \text{CO}}$, $\sigma_{\text{H}_2, \text{CO}}$, and $\sigma_{d, \text{CO}}$ are cross sections for the CO photodissociation, shielding by H₂ molecules, and the dust absorption. Equation (17) is integrated as,

$$F_{\nu, \text{CO}} = \frac{S_{\nu, \text{CO}}}{4\pi r^2} \exp(-\tau_{\nu, \text{CO}}), \quad (18)$$

where $\tau_{\nu, \text{CO}}$ is,

$$\tau_{\nu, \text{CO}} = \int n (X_{\text{CO}} Z_C \sigma_{\nu, \text{CO}} + 0.5 X_{\text{H}_2} \sigma_{\text{H}_2, \text{CO}} + \sigma_{d, \text{CO}}) dr. \quad (19)$$

van Dishoeck & Black (1988) have listed about 30 lines to photodissociate CO molecules in the energy range of $11.0 \text{ eV} < h\nu < 13.6 \text{ eV}$. As for the H₂ molecule Lyman bands, we use the typical one line, $\sigma_{\nu, \text{CO}}$ to calculate the photodissociation rate of CO molecules. We adopt the Voigt profile given by (14) and (15) again, and make up the representative line with typical parameters ; $h\nu_0 = 12.925 \text{ eV}$ ($\lambda_0 = 960 \text{ \AA}$), $\gamma = 1.0 \times 10^{-11} \text{ s}^{-1}$ and $f = 0.01$ respectively. We put the logarithmic grids at $12.88 \text{ eV} < h\nu < 12.96 \text{ eV}$ to get the resolution higher around the line center. The radiation field, $S_{\nu, \text{CO}}$ in equation (18) is determined in the same manner as S_{ν, H_2} . In the PDR, CO molecules are shielded by the dust and H₂ molecules. Lee et al. (1996) have calculated the shielding function by the dust and H₂ molecules for the CO photodissociation rate. We have found that their results (Table 11) can be approximated with some analytic functions. Their dust attenuation law can be fitted with $\exp(-3.5A_V)$ within a factor of 2 at $A_V < 7$. Similarly, their H₂ molecule shielding function can be fitted with $\exp(-N_{\text{H}_2}/1.6 \times 10^{21} \text{ cm}^{-2})$ within 20% error at $N_{\text{H}_2} < 8 \times 10^{21} \text{ cm}^{-2}$. Therefore, we adopt the corresponding cross sections in our calculations, $\sigma_{d, \text{CO}} = 1.7 \times 10^{-21} \text{ cm}^2$ and $\sigma_{\text{H}_2, \text{CO}} = 6.25 \times 10^{-22} \text{ cm}^2$ respectively. Fig.2 shows the cross sections for the CO photodissociation rate. As this figure shows, the self-shielding effect is not so significant owing to the small abundance of C atoms. The dust cross section is largest in most of the energy range, which means that CO molecules are mainly shielded by the dust absorption.

Finally, we define the frequency-integrated FUV photon number flux normalized with the Habing’s unit, G_{FUV} (Habing 1968). We assume that G_{FUV} is attenuated only by the dust absorption,

$$\frac{1}{r^2} \frac{\partial(r^2 G_{\text{FUV}})}{\partial r} = -n\sigma_{\text{d}} G_{\text{FUV}}, \quad (20)$$

which is solved as,

$$G_{\text{FUV}} = \frac{1}{F_{\text{H}}} \frac{S_{\nu, \text{FUV}}}{4\pi r^2} \exp(-\tau_{\text{d}}), \quad (21)$$

where F_{H} is the Habing field, $F_{\text{H}} = 1.21 \times 10^7 \text{ cm}^{-2}\text{s}^{-1}$ (Habing 1968; Bertoldi & Draine 1996), and τ_{d} is the dust optical depth defined as,

$$\tau_{\text{d}} = \int n\sigma_{\text{d}} dr. \quad (22)$$

We adopt $\sigma_{\text{d}} = 1.2 \times 10^{-21} \text{ cm}^{-2}$, which is the average value between 1000 and 2000 Å and corresponds to the attenuation law of $\exp(-2.5A_{\text{V}})$ (Roberge et al. 1991). As mentioned above, we assume $\sigma_{\text{d}} = 0$ in the H II region for simplicity. We use this flux, G_{FUV} to calculate the photoelectric heating and dust recombination cooling rate (Bakes & Tielens 1994), reformation rate of CO molecules (Nelson & Langer 1997), and dust temperature (Hollenbach, Takahashi & Tielens 1991).

2.1.3. Chemical Reaction Equations

Non-equilibrium reaction equations are solved for the species of e, H, H^+ , H_2 , C^+ , and CO. The ionization rate of O is assumed to be the same as that of H. We adopt the solar elemental abundances with some depletions, $Y_{\text{He}} = 0.1$, $Z_{\text{O}} = 5.4 \times 10^{-4}$, and $Z_{\text{C}} = 2.3 \times 10^{-4}$ (Hollenbach & McKee 1989).

We solve the minimal set of chemical reactions listed in Table 2. The main reactions in the H II region are the photoionization by the UV photons from the central star and the recombination. In the PDR, the FUV photons photodissociate H_2 and CO molecules. The reformation of H_2 molecules mainly occurs on the surface of dust grains. The dissociation and reformation of CO molecules is approximated with the direct process between CO and C^+ (Nelson & Langer 1997).

Below, we show the photoionization and photodissociation rates, which relate to the transfer equations explained in §2.1.2. The photoionization rates of H and H_2 , photodissociation rates of H_2 and CO molecules are,

$$\frac{dX_{\text{H}^+}}{dt} = -\frac{dX_{\text{H}}}{dt} = X_{\text{H}} \int_{\nu_{\text{Ly}\alpha}}^{\infty} \sigma_{\nu, \text{UV}} F_{\nu, \text{UV}} d\nu', \quad (23)$$

Table 2. Included Chemical Processes

species	reactions	reference	note
H \rightarrow H ⁺	photoionization	see §2.1.3	
	collisional ionization	1	
	cosmic-ray	2	
H ⁺ \rightarrow H	recombination	3	
H ₂ \rightarrow H ⁺	photoionization	see §2.1.3	
	cosmic-ray	2	
H ₂ \rightarrow H	photodissociation	see §2.1.3	
	cosmic-ray	2	
H \rightarrow H ₂	reformation	4	
	gas-phase reaction	4	†1
CO \rightarrow C ⁺	photodissociation	see §2.1.3	
C ⁺ \rightarrow CO	reformation	5	

REFERENCES—(1) Tenorio-Tagle 1986, (2) Wolfire et al. 1995, (3) , (4) Hollenbach & McKee 1979 (HM79), (5) Nelson & Langer 1997 NOTES—†1 : we use the rate by HM79 for reactions; H + e \rightarrow H⁻ + γ and H⁻ + H \rightarrow H₂ + e

$$\frac{dX_{\text{H}^+}}{dt} = -2\frac{dX_{\text{H}_2}}{dt} = 2X_{\text{H}_2} \int_{\nu_{\text{Ly}1}}^{\infty} \sigma_{\nu,\text{UV}} F_{\nu,\text{UV}} d\nu' , \quad (24)$$

$$\frac{dX_{\text{H}}}{dt} = -2\frac{dX_{\text{H}_2}}{dt} = 2X_{\text{H}_2} \int_{\nu_-}^{\nu_+} \frac{p_{\text{dis}}}{1 - f_{\text{rem}}} \sigma_{\nu,\text{H}_2} F_{\nu,\text{H}_2} d\nu' , \quad (25)$$

$$\frac{dX_{\text{C}^+}}{dt} = -\frac{dX_{\text{CO}}}{dt} = X_{\text{CO}} \int_{\nu_-}^{\nu_+} \sigma_{\nu,\text{CO}} F_{\nu,\text{CO}} d\nu' , \quad (26)$$

where p_{dis} in equation (25) is the probability that the pumped H₂ molecules are photodissociated, decaying to $X^1\Sigma_g^+$. We adopt the average value, $p_{\text{dis}} = 0.15$ (Draine & Bertoldi 1996). The integration in equations (25) and (26) are done in the considered frequency range around our representative lines. As equation (24) shows, we assume that if UV photons (> 13.6 eV) reach the molecular region, one H₂ molecule is directly ionized to two H⁺ ions as two H atoms are photoionized.

2.2. Thermal Processes

We include 5 heating processes and 12 cooling processes in the energy equation. These processes are listed in Table 3. In Table 3, heating/cooling processes are divided into pro-

Table 3. Included Thermal Processes

	region	process	reference	note	
Heating	HII	H photoionization	1 etc.		
	PDR	Photoelectron from dust	2		
		H ₂ photodissociation	3		
		H ₂ reformation	3		
		Cosmic-ray	4		
Cooling	HII	H recombination	1 etc.		
		Lyman- α	1		
		OI (63.0 μ m)	5		
		OII (37.29 μ m)	5		
		CII (23.26 μ m)	5		
			Collisional ionization	6	
	PDR	OI (63.1 μ m)	5, 7	†1	
		CII (157.7 μ m)	5, 7	†1	
		H ₂ rot/vib excitation	3, 8		
		CO rot/vib excitation	3		
Dust recombination		2			
		Collisional dust-gas heat transfer	5	†2	

REFERENCES—(1) Spitzer 1978, (2) Bakes & Tielens 1994, (3) Hollenbach & McKee 1977, (4) Shull & Van Steenberg 1985, (5) Hollenbach & McKee 1989, (6) Tenorio-Tagle 1986, (7) Tielens & Hollenbach 1985, (8) Galli & Palla 1998. NOTES—†1 : these can be a heating process when the background radiation is greater than the source function. †2 : this can be a heating process when the dust temperature is higher than the gas temperature.

cesses dominant in the H II region or PDR. In the H II region, the included heating process is photoionization heating of hydrogen atoms. The main cooling processes in the H II region are recombination cooling and some meta-stable atomic lines (e.g., [O II] 3729 Å, [C II] 2326 Å). We do not include the photoelectric heating in the H II region, because this is sensitive to the uncertain abundance of small grains. We do not include the line cooling with highly ionized ions (e.g., [O III], [C III] etc.) either. We are interested in the boundary region between the H II region and the molecular cloud, and thus we do not solve the detailed ionization structure in the H II region.

In the PDR, the main heating process is photoelectric heating. We separately list the dust recombination cooling, which exceeds the photoelectric heating at high temperatures ($T > 10^3$ K, Bakes & Tielens 1994). In our calculation, cosmic-ray heating is important only in the outer molecular region, where the FUV flux from the central star is significantly reduced by geometrical dilution and dust extinction. The main cooling processes in the PDR are fine-structure atomic lines of [O I] 63.1 μm and [C II] 157.7 μm , which are the characteristic lines of the PDR (e.g., Hollenbach & Tielens 1999). The [O I] 63.1 μm is more efficient than [C II] 157.7 μm at high density ($n \geq 10^4$ cm $^{-3}$), and it is the reverse at the low density ($n \leq 10^2$ cm $^{-3}$). We do not include [CI] 370 μm and 609 μm transitions because we adopt the approximate treatment that CO molecules are directly photodissociated to C $^+$ (Nelson & Langer 1997). The rotational transitions of CO molecules are the primary cooling process in the molecular region. Collisional heat transfer between gas and dust is important when the density is very high ($> 10^5$ cm $^{-3}$). If dust temperature is higher than the gas temperature, this process heats up the gas.

2.3. Dust Temperature

We calculate the dust temperature following the approximation method by Hollenbach, Takahashi & Tielens (1991). In our calculation, several thermal processes depend on the dust temperature. Dust IR emission affects the level population of atoms and cooling rates with line transitions (e.g., [OI] 63.1 μm and [C II] 157.7 μm). If the intensity of the IR dust emission at the line frequency exceeds the source function of the line, this transition works as a heating process rather than a cooling process. The collisional dust-gas heat transfer rate is proportional to the difference between the gas and dust temperature.

3. Calculation Procedures

3.1. Outline

Our numerical scheme for the hydrodynamics is based on the 2nd-order Lagrangian Godunov method (see, e.g., van Leer 1979). First, we explicitly integrate the continuity equation and the momentum equation to obtain the new position of the cell, r_j^{n+1} , gas density, ρ_j^{n+1} , and velocity, u_j^{n+1} , where the indices j and n refer to different steps in space and time respectively. Next, we iteratively solve the chemical rate equations and the energy equation. The energy equation (3) is transformed with equations (2), (4) and (5) as,

$$\begin{aligned} \frac{dT}{dt} &+ \frac{T}{2w} \left(\frac{dX_{\text{H}}}{dt} + 3\frac{dX_{\text{H}^+}}{dt} \right) \\ &+ \frac{\mu m_{\text{H}}(\gamma - 1)}{kw} \left\{ ur^2 \frac{\partial p}{\partial m} - \frac{\partial(r^2 up)}{\partial m} - \frac{\partial(r^2 q_{\text{cond}})}{\partial m} \right\} \\ &= \frac{\gamma - 1}{kw} (\Gamma - \Lambda), \end{aligned} \quad (27)$$

where w is defined as,

$$w \equiv 0.5(1 + X_{\text{H}} + 3X_{\text{H}^+}) + Y_{\text{He}}. \quad (28)$$

The terms with m -derivative are explicitly calculated before the iteration. The different rate equations and energy equation include the new gas temperature, T_j^{n+1} , dust temperature, $T_{\text{d},j}^{n+1}$, and chemical compositions, $X_{s,j}^{n+1}$ (s : species). We determine these quantities by means of the Newton-Raphson method. After the iteration converges, the gas pressure and UV/FUV flux are calculated using the newly obtained gas density, temperature, and compositions. The integration proceeds from the center to the outer cells.

3.2. Initial Condition

The hydrodynamical expansion of the H II region occurs after the IF passes the initial Strömgen radius (expansion phase). We start our calculation when the H II region is still in the previous formation phase. In the formation phase, the timescale of the system is very short and the expanding H II region hardly affects the gas dynamics. At $t = 0$, we set the constant mass density and no initial velocity field. We set the initial H II region ($X_{\text{H}^+} = X_{\text{C}^+} = 1$, $T = 10^4$ K) at $r < R_{\text{st}}/5$. The outer initial PDR ($X_{\text{H}} = X_{\text{C}^+} = 1$, $T = 100$ K) and the molecular region ($X_{\text{H}_2} = X_{\text{CO}} = 1$, $T = 10$ K) is set at $R_{\text{st}}/5 < r < 2R_{\text{st}}/5$ and $r > 2R_{\text{st}}/5$ respectively.

Table 4. Model Parameters

Model	M_* (M_\odot) ^a	$n_{\text{H},0}$ (cm^{-3}) ^b	R_{st} (pc) ^c	t_{dyn} (Myr) ^d
S101	101.3	10^3	1.27	0.12
S41 ^e	40.9	10^3	0.56	0.05
LD-S41	40.9	10^2	2.53	0.23
HD-S41	40.9	10^4	0.12	0.011
S19	19.0	10^3	0.25	0.023
S12	11.7	10^3	0.04	0.004

a : mass of the central star, b : number density of the ambient gas, c : initial Strömgen radius, d : dynamical time, $R_{\text{st}}/C_{\text{HII}}$, where C_{HII} is the sound speed at $T = 10^4$ K. e : Our model for Sh104 (Paper I).

3.3. Time Step

The time step of the calculation, Δt , is constrained by some conditions. The first one is the normal Courant condition,

$$\Delta t_{\text{c},j} = \frac{\Delta r_j}{C_{\text{s},j}}, \quad (29)$$

where $C_{\text{s},j}$ is the sound speed at the j-th cell. We include the thermal conduction explicitly in the energy equation, and we have another Courant condition,

$$\Delta t_{\text{cond},j} = \frac{1}{2} \frac{p_j}{K_j T_j (\gamma - 1)} (\Delta r_j)^2, \quad (30)$$

where K_j is the conductivity calculated with equation (B2) to satisfy the Field condition. Besides these Courant conditions, Δt is constrained by the velocity of the IF. In the early formation phase of the H II region, the IF expands supersonically. Since the ionization rate and the temperature change sharply at the IF, Δt must be short enough that the IF advances less than the width of one cell, Δr_j in one time step, Δt .

We choose the minimum time step from among the above time steps to determine Δt . In the early formation phase, Δt is mainly constrained by the expanding velocity of the IF. In the next expansion phase, when the SF emerges, the Courant conditions limit the time step.

4. Dependence on Ambient Number Density

4.1. Models

In this section, we show how the time evolution of the H II region, PDR, and the swept-up shell changes with different ambient number densities. For comparison, we calculate the expansion of the H II region around the $41M_{\odot}$ star, which is the central star of Sh104 modeled in Paper I, but with different ambient number densities. As we have adopted the ambient number density of $n_{\text{H},0} = 10^3 \text{ cm}^{-3}$ in Paper I, we show the results of the higher density case, $n_{\text{H},0} = 10^4 \text{ cm}^{-3}$ and the lower density case, $n_{\text{H},0} = 10^2 \text{ cm}^{-3}$ below. The initial Strömgen radius and the dynamical time for the calculated models are listed in Table 4. All the other conditions are the same as those in our model of Sh104 (S41 in Table 4) except for the number density.

4.2. Scaling Relations

First, we show some scaling relations that are very useful to interpret the numerical results. The initial Strömgen radius depends on the ambient number density, and other relevant quantities are also scaled as,

$$R_{\text{st}} \propto n^{-2/3}, \quad (31)$$

$$t_{\text{dyn}} = R_{\text{st}}/C_{\text{HII}} \propto n^{-2/3}, \quad (32)$$

$$M_{\text{sh}} \propto nR_{\text{st}}^3 \propto n^{-1}, \quad (33)$$

$$N_{\text{sh}} \propto nR_{\text{st}} \propto n^{1/3}, \quad (34)$$

$$F_{\text{FUV},i} \propto S_{\text{FUV}}/R_{\text{st}}^2 \propto n^{4/3}, \quad (35)$$

where M_{sh} and N_{sh} is the mass and the column density of the shell, $F_{\text{FUV},i}$ is the incident FUV flux at the IF at a given t/t_{dyn} . To derive the above relations, we assume that most of the swept-up gas remains in the shell, which is a good approximation for expansion in a homogeneous ambient medium. As (31) and (32) show, the larger H II region expands in the lower density ambient medium over a longer timescale. Equation (33) shows that the swept-up mass is larger with the lower density medium. The shell structure is mainly determined by the column density of the shell, N_{sh} and the FUV flux at the IF, $F_{\text{FUV},i}$. The detailed properties of the shell are explained with equation (34) and (35) in §4.3.

4.3. Results of Numerical Calculations

Figures 3 and 4 show the hydrodynamical evolution of models HD-S41 and LD-S41 respectively. Since the Strömgren radius is smaller for the higher ambient density, the H II region expands to the region of ~ 1 pc in HD-S41, and ~ 20 pc in model LD-S41 in $t \sim 20 t_{\text{dyn}}$. As expected with equation (32), the timescale of the evolution is longer for the lower density model. The time of $20 t_{\text{dyn}}$ corresponds to ~ 0.25 Myr for HD-S41, and ~ 5 Myr for model LD-S41.

The basic time evolution is the same as that of model S41 (Paper I). The SF emerges when the IF reaches the initial Strömgren radius. The gas density within the shell is about 10-100 times as high as that of the ambient medium, though the detailed structure of the shell differs between HD-S41 and LD-S41 (explained below). The time evolution after the SF emerges is also similar to that of model S41. The time evolution of the radial expansion is well approximated with,

$$R_{\text{IF}}(t) = R_{\text{st}} \left(1 + \frac{7}{4} \sqrt{\frac{4}{3}} \frac{C_{\text{II}} t}{R_{\text{st}}} \right)^{4/7}, \quad (36)$$

which is derived from the equation of motion of the shell,

$$\frac{d}{dt} \left(\frac{4\pi}{3} R_{\text{IF}}^3 \rho_0 \dot{R}_{\text{IF}} \right) = 4\pi R_{\text{IF}}^2 p_{\text{II}} = 4\pi R_{\text{IF}}^2 \rho_0 C_{\text{II}}^2 \left(\frac{R_{\text{st}}}{R_{\text{IF}}} \right)^{3/2}, \quad (37)$$

where ρ_0 is the mass density of the ambient medium, and p_{II} is the gas pressure in the H II region. Equation (36) is different from the well-known expansion law (e.g., Spitzer 1978) by a factor of $\sqrt{4/3}$, but shows better agreement with the numerical results. As equation (37) shows, equation (36) does not involve the detailed structure and the chemical composition of the shell, which we analyze with our numerical calculations. The swept-up mass in the shell is larger for the lower ambient number density, as equation (33) shows. For example, $M_{\text{sh}} \sim 10^5 M_{\odot}$ in model LD-S41 and $M_{\text{sh}} \sim 10^3 M_{\odot}$ in model HD-S41 at $t \sim 20 t_{\text{dyn}}$ respectively. The upper panels of Fig.5 and 6 show the time evolution of various front positions. Initially, the DFs expand more rapidly than the SF and the IF, then the PDR appears in front of the SF. As the H II region expands, the IF and the SF gradually overtake the preceding DFs of H₂ and CO in turn. Finally the DFs are taken up into the shell. The SF enters the molecular region, and the molecular gas is accumulated within the shell. The rapid reformation within the shell also helps to accelerate the accumulation of the molecular gas.

The main difference among these models is the time (or t/t_{dyn}) when the DFs are taken into the shell. In the higher density model, HD-S41, the IF and the SF catch up with both

DFs of H₂ and CO by the time of 5 t_{dyn} . In the lower density model, LD-S41, the DF of H₂ is quickly taken into the shell, but the accumulation of CO molecules is delayed. The DF of CO is taken into the shell at $t \sim 20 - 30 t_{\text{dyn}}$ in model LD-S41. About 70% (90%) of carbon (hydrogen) atoms within the shell exist as CO (H₂) molecules in model HD-S41 at $t \sim 20 t_{\text{dyn}}$, but 20% (90%) in model LD-S41 at the same time step. We explain the reasons for this difference below. With the higher ambient number density, the incident FUV flux at the IF is strong, as equation (35) shows. Although the FUV photons are available to photodissociate molecules, our calculation shows that the FUV photons are quickly shielded in model HD-S41. This is because the column density of the shell, N_{sh} is larger for the higher density model, as equation (34) shows. Fig.7 is a schematic picture showing the density-dependence of N_{sh} and $F_{\text{FUV},i}$. The incident FUV flux is attenuated enough by the dust extinction through the shell, and the molecular gas is reliably protected in the outer part of the shell. Though the density-dependence of N_{sh} , $N_{\text{sh}} \propto n^{1/3}$, is weaker than that of $F_{\text{FUV},i}$, $F_{\text{FUV},i} \propto n^{4/3}$, the dust absorption becomes significant with a high number density owing to the attenuation law of $\exp(-\sigma_{\text{d}}N_{\text{sh}})$. The lower panels of Fig.5 shows the time evolution of the column density of each region in model HD-S41. The column density of the shell at $t \sim 5 t_{\text{dyn}}$ is already $N_{\text{sh}} \sim 4 \times 10^{21} \text{ cm}^{-2}$ ($A_{\text{V,sh}} \sim 2$) in this model. In model LD-S41, on the other hand, the incident FUV flux is weak, but the column density of the shell is low. Since the CO molecules are mainly shielded by the dust absorption, it is not until N_{sh} becomes somewhat large ($A_{\text{V,sh}} \sim 1$) that CO molecules are accumulated in the shell. However, even in the early phase when $A_{\text{V,sh}} < 1$, H₂ molecules can be quickly accumulated in the shell, as Fig.6 shows. This is due to the efficient self-shielding of H₂ molecules. Hollenbach & Tielens (1999) have briefly shown that H₂ molecules can be self-shielded, if $G_{\text{FUV}}/n \leq 4 \times 10^{-2}$ at the IF. In our calculations, $G_{\text{FUV}}/n \sim 1.6 \times 10^{-2}$ in model LD-S41 and $G_{\text{FUV}}/n \sim 0.5$ in model HD-S41 at $t \sim 5 t_{\text{dyn}}$. Therefore, H₂ molecules are mainly self-shielded in model LD-S41, and shielded by the dust in model HD-S41 respectively. The self-shielding effect for CO molecules is not so efficient, owing to the small abundance of carbon atoms.

The detailed structure of the shell differs significantly among these models. Fig.8 (Fig.9) shows the detailed structure of the density and the temperature within the shell at $t \sim 15 t_{\text{dyn}}$ in model HD-S41 (LD-S41). These figures show that the gas temperature in the inner region of the shell is higher in the model with the higher ambient density; $T_{\text{HI}} \sim 500 \text{ K}$ in model HD-S41 and $T_{\text{HI}} \sim 50 \text{ K}$ in model LD-S41. This is because the FUV flux at the IF, $F_{\text{FUV},i}$ is larger for the higher ambient density owing to the smaller Strömgren radius (see eq.(35)). The FUV radiation field, G_{FUV} defined by eq.(21) at the IF is $G_{\text{FUV}} \sim 10$ in LD-S41 and ~ 5000 in HD-S41 at the time step of both figures, $t \sim 15 t_{\text{dyn}}$. Within the shell, the temperature has a negative gradient and the density has a positive gradient, which is similar to model S41 (Paper I). Figs.8 and 9 show that the changes in gas temperature and density

are milder in model LD-S41. The gas temperature decreases from 500 K to 25 K through the shell in model HD-S41 and from 50 K to 25 K in model LD-S41. These differences are also explained in equation (34) and (35). In model HD-S41, the FUV flux is strong and the column density is high. The intense FUV radiation is shielded by the shell with the large column density. In model LD-S41, the incident FUV flux at the IF is relatively weak and the column density of the shell is low. The gas temperature within the shell is lower and nearly constant. The FUV flux is attenuated from $G_{\text{FUV}} \sim 5000$ to 0.1 through the shell in HD-S41, and from $G_{\text{FUV}} \sim 10$ to 1.5 in LD-S41 at the time of Fig.8 and 9. In model HD-S41, the gas temperature significantly decreases toward the outer part of the shell, because the photoelectric heating becomes inefficient. Conversely, the gas density of the outer region of the shell rises to $n \sim 10^6 \text{ cm}^{-3}$. The collisional heat transfer between the gas and dust is efficient there, and the gas temperature is almost equal to the dust temperature. The swept-up shell is geometrically thicker in model HD-S41. Figs.8 and 9 also show that the density jump at the IF is larger with the lower ambient density. This can be explained by the analytic jump condition at the weak D-type IF,

$$\frac{\rho_{\text{HII}}}{\rho_{\text{HI}}} = \frac{C_{\text{I}}^2}{2C_{\text{II}}^2}(1 + \delta) \sim \frac{T_{\text{HI}}}{T_{\text{HII}}} \quad (38)$$

(Mihalas & Mihalas 1984), where C_{I} and C_{II} are the sound speed ahead and behind the IF, and δ is the quantity less than unity. Since the temperature T_{HI} is lower for the lower ambient density, the density at the inner edge of the shell is higher in model LD-S41.

4.4. Fragmentation of the Shell

It is important to know whether or not the swept-up molecular layer fragments, as the triggered star formation scenario predicts. We do not consider the dynamical instability, but only the gravitational instability for the fragmentation of the shell, as discussed in Paper I. In the lower panels of Figs.5 and 6, the shaded region is the expected unstable region, where $t > (G\rho)^{-1/2}$. The swept-up shell in each model is expected to suffer from gravitational instability. The unstable region spreads from the outer edge of the shell, which is the same as in model S41 (Paper I). In model HD-S41, the density is relatively low in the inner part of the shell. The unstable region appears at $t \sim 0.08 \text{ Myr}$ ($7.3 t_{\text{dyn}}$) and gradually extends from the cold molecular layer, as Fig.5 shows. As explained in the previous subsection, both H_2 and CO molecules are shielded by the dust, and the shell is dominated by these molecules when the shell becomes unstable. In model LD-S41, the swept-up shell is relatively cold and dense (see Fig.9). The unstable region rapidly spreads in the whole shell at $t \sim 1.5 \text{ Myr}$ ($6.5 t_{\text{dyn}}$). In this model, the shell is dominated by H_2 molecules due to the efficient self-shielding effect by the time of the shell-fragmentation. However, the column density of the

shell is still not high enough to protect CO molecules by the dust extinction in the early expansion phase. The accumulation of CO molecules begins after the shell becomes unstable, which is different from model HD-S41. Regardless of some differences, the expanding H II region can sweep up the molecular gas, and the fragmentation of the shell is finally expected with different number densities. The star formation will be triggered in the fragmented shell along the lines of a “collect and collapse” scenario.

5. Dependence on the Central Star

5.1. Models

In this section, we investigate how the time evolution of the H II region, PDR, and the shell depends on the UV/FUV luminosity (mass) of the central star. For this purpose, we calculate the expansion around the central star of $101.3M_{\odot}$, $19.0M_{\odot}$ and $11.7M_{\odot}$ as representative cases. We use the same ambient number density, $n_{\text{H},0} \sim 10^3 \text{ cm}^{-3}$, as in model S41 (Paper I). Model parameters of these calculated models are listed in Table 4.

5.2. Scaling Relations

The less massive central star has smaller UV and FUV luminosities, but a large luminosity ratio, $S_{\text{FUV}}/S_{\text{UV}}$ (see Table 1). The Strömgen radius depends on the UV photon number luminosity, S_{UV} , as well as the number density, so that other relevant quantities also depend on S_{UV} . The scaling relations which are similar to equation (31) – (35) are derived as,

$$R_{\text{st}} \propto S_{\text{UV}}^{1/3}, \quad (39)$$

$$t_{\text{dyn}} = R_{\text{st}}/C_{\text{HII}} \propto S_{\text{UV}}^{1/3}, \quad (40)$$

$$M_{\text{sh}} \propto nR_{\text{st}}^3 \propto S_{\text{UV}}, \quad (41)$$

$$N_{\text{sh}} \propto nR_{\text{st}} \propto S_{\text{UV}}^{1/3}, \quad (42)$$

$$F_{\text{FUV},i} \propto S_{\text{FUV}}/R_{\text{st}}^2 \propto (S_{\text{FUV}}/S_{\text{UV}})^{2/3} S_{\text{FUV}}^{1/3}, \quad (43)$$

where M_{sh} , N_{sh} , and $F_{\text{FUV},i}$ are the quantities at a given t/t_{dyn} . As equation (39) and (40) show, the H II region expands into the larger region on a longer timescale, as the mass of the central star increases. The FUV flux at the IF, $F_{\text{FUV},i}$ depends on both the luminosity ratio, $S_{\text{FUV}}/S_{\text{UV}}$ and the FUV luminosity, S_{FUV} . Since the dependence on the luminosity ratio is stronger than that on the FUV luminosity, the FUV flux, $F_{\text{FUV},i}$ becomes larger for

the lower mass central star. The calculated shell structure reflects the column density, N_{sh} (eq.(42)) and the FUV flux at the IF, $F_{\text{FUV},i}$, (eq.(43)) which is explained in §5.3.

5.3. Results of the Numerical Calculation

Figs.10, 11, and 12 show the hydrodynamical evolution of models S101, S19, and S12 respectively. The basic time evolution features are similar among these models. When the IF reaches the initial Strömngren radius, the SF emerges in front of the IF. In all these models, the H II region expands into the region of $\sim 1 - 10$ pc over a timescale of ~ 1 Myr. However, the time normalized with t_{dyn} differs considerably among these models, because t_{dyn} decreases as the UV luminosity decreases (eq. (40)). For example, the time of 1 Myr corresponds to $\sim 8 t_{\text{dyn}}$ in model S101, $\sim 40 t_{\text{dyn}}$ in model S19, and $\sim 300 t_{\text{dyn}}$ in model S12. Figs.10 - 12 all show that the PDR initially appears in front of the SF and is finally taken into the shell over a timescale of $\sim 1 - 2$ Myr; such evolution is largely different in terms of time normalized with t_{dyn} .

These differences are explained using equations (42) and (43). As equation (43) shows, the FUV flux at the IF at a given t/t_{dyn} , $F_{\text{FUV},i}$ is larger with the less massive star. Conversely, the column density of the shell, N_{sh} is smaller for the less massive star, shown in equation (42). At $t \sim 10 t_{\text{dyn}}$, for example, $G_{\text{FUV}} \sim 100$ at the IF and $N_{\text{sh}} \sim 3 \times 10^{21} \text{ cm}^{-2}$ in model S19, and $G_{\text{FUV}} \sim 600$ and $N_{\text{sh}} \sim 7 \times 10^{20} \text{ cm}^{-2}$ in model S12. Therefore, the strong FUV radiation is not shielded, and the reformed molecules are easily photodissociated. Fig.16 is the schematic picture showing the luminosity-dependence of N_{sh} and $F_{\text{FUV},i}$. The accumulation of molecular gas in the shell is significantly delayed on t/t_{dyn} . The upper panels of Figs.13 - 15 show the time evolution of the various front positions in each model. Both DFs of H_2 and CO molecules are taken into the shell by the time of $4 t_{\text{dyn}}$ in model S101, $45 t_{\text{dyn}}$ in model S19, and $550 t_{\text{dyn}}$ in model S12. The times of the front overtaking are totally different at t/t_{dyn} , but these times differ only by a factor of a few at time t ; $t \sim 0.4$ Myr in model S101, $t \sim 1$ Myr in model S19, and ~ 2 Myr in model S12. Eventually, sufficient molecular gas always gathers in the outer region of the shell in a few Myrs with the ambient number density of $n_{\text{H},0} \sim 10^3 \text{ cm}^{-3}$. The total mass of the swept-up shell (between the IF and the SF) is $3.5 \times 10^4 M_{\odot}$, $9.8 \times 10^3 M_{\odot}$, and $3.8 \times 10^3 M_{\odot}$ in models S101, S19, and S12 respectively at the final time step of Figs.13 - 15. At that time step, more than 85% of hydrogen atoms are included in H_2 molecules in all models. The fraction of CO molecules is 55%, 40%, and 20% in each respective model.

The upper panel of Fig.17 shows the time evolution of the maximum density of the shell in models S101, S41, S19 and S12. As this figure shows, the swept-up shell is always denser

with the more massive central star. This is explained with the time evolution of the velocity of the shell. The expansion of the H II region approximately follows equation (36), and the expansion velocity decreases as,

$$\dot{R}_{\text{IF}}(t) = \sqrt{\frac{4}{3}} C_{\text{HII}} \left(1 + \frac{7}{4} \sqrt{\frac{4}{3}} \frac{t}{t_{\text{dyn}}} \right)^{-3/7}, \quad (44)$$

because the gas pressure of the H II region decreases. In model S101, the FUV radiation is easily shielded because of the high column density of the shell. The photoelectric heating outside the shell becomes inefficient, and the gas temperature in front of the SF quickly decreases. At that time, t/t_{dyn} is still small, and the expansion velocity is still large according to equation (44). The Mach number of the SF is large, $\mathcal{M} \sim 10$. In model S12, it takes hundreds of t_{dyn} to shield the FUV radiation by the dust extinction through the shell. The expansion velocity significantly decreases by (44), and the Mach number is only about a few. This difference causes a different shell density in each model, because the density jump at the isothermal SF is proportional to \mathcal{M}^2 . The lower panel of Fig.17 presents the time evolution of the Mach number in each model. This figure clearly shows that the Mach number is larger in the model with the more massive central star.

During the expansion, the pressure gradient in the PDR outside the shell hardly affects the hydrodynamics. The pressure gradient outside the shell gradually disappears as the FUV photons are shielded by the dust in the shell. The SF does not emerge in front of the DFs in our calculations.

5.4. Fragmentation of the Shell

Even with different central stars, the molecular gas is finally accumulated in the swept-up shell. The lower panels of Figs.13, 14, and 15 show the time evolution of the column density of each region in models S101, S19, and S12 respectively. In all these models, the number density of the molecular layer finally becomes over ten times as high as the ambient density, and gravitational fragmentation is expected there. In Figs.13 - 15, the shaded region is the unstable region expected in each model, where $t > (G\rho)^{-1/2}$. As shown in these figures, the unstable region spreads in the shell, as the DFs of CO are taken into the shell. The unstable region appears at $t \sim 0.2$ Myr in model S101, $t \sim 0.5$ Myr in model S19, and $t \sim 1.1$ Myr in model S12. As explained in the previous subsections, these times are largely different at t/t_{dyn} ; ~ 2 in model S101, ~ 20 in model S19, and ~ 300 in model S12. The FUV flux at the IF is stronger with the less massive star, and it takes a long time in t_{dyn} units to form the dense molecular layer shielding the FUV radiation field.

6. Discussions

6.1. Dust Grains

6.1.1. Dust Grains in H II Region

In the above calculations, we have not included the dust grains in the H II regions to avoid uncertainties (e.g., size distribution), but some observations indicate their presence (e.g., see Spitzer 1978). The dust absorption of the UV and FUV radiation will decelerate the propagation of the IF and DFs and affect the structure of the swept-up shell. Weingartner & Draine (2001) have noted that the photoelectric heating can be as important as the photoionization heating, even in the H II region. The importance of the dust absorption in the H II region is often evaluated with the column density of the dust-free static H II region,

$$N_{\text{HII}} \propto nR_{\text{st}} \propto n^{1/3} S_{\text{UV}}^{1/3} \quad (45)$$

(Petrosian et al. 1972; Arthur et al. 2004), where R_{st} is the dust-free Strömngren radius, n is the ambient number density, and S_{UV} is the UV photon number luminosity of the central star. The radius of the corresponding dusty H II region is smaller for larger N_{HII} . Arthur et al. (2004) has also shown that the dust absorption in the H II region gradually becomes inefficient, as the H II region dynamically expands.

In order to evaluate the effect of the dust in the H II region, we have calculated some models including the dust in the H II region as well as the outer PDR. In models S41-HD and S41-LD, the radius of the H II region and PDR decreases only by 10% and 3% compared with the dust-free counterparts. In models S101 and S41, the reduction of each region is 20% and 5% of the dust-free radius. These results agree with equation (45), which shows that the dust absorption in the H II region becomes significant with the higher ambient number density, or the more massive central star. In all of the above calculations, however, the dust absorption in the H II region is not so significant. Furthermore, the dust in the H II region also absorbs FUV photons in addition to UV photons. As briefly mentioned in Paper I, this only slightly promotes the accumulation of molecules in the shell. Therefore, dust grains in the H II region hardly affect our conclusions. The dust absorption in the H II region is more important in the denser and more compact region (e.g., ultra compact H II region), where the detailed treatment of grains is required.

6.1.2. *Reformation of Hydrogen Molecules on Grain Surface*

The reformation of H_2 molecules on the grain surface is one of the key processes in our calculations. The FUV radiation is consumed in photodissociating the reformed molecules in the shell, which accelerates the accumulation of H_2 molecules. However, there still remain uncertainties in the reformation rate, which depends on the detailed behavior of H atoms and H_2 molecules on the grain surface. At high dust temperatures, for example, H atoms absorbed on the grain surface evaporate before the reformation of H_2 molecules. The critical temperature, T_{cr} , is about 20 K on pure grains, but Hollenbach & Salpeter (1971) have shown that the irregular surface with impurity sites raises T_{cr} to $25 \text{ K} < T_{\text{cr}} < 50 \text{ K}$. Recently, Cazaux & Tielens (2002, 2004) have refined the absorption process of H atoms on the grain surface, and obtained a much higher critical temperature of $T_{\text{cr}} \sim 100 \text{ K}$. In our calculations presented in §4 and 5, we have not included the high-temperature cut-off in the reformation rate, for simplicity. We analyze the validity of this treatment here.

We calculate some models including the cut-off using the functional form given by Hollenbach & McKee (1979) (HM79). In each model, two cases of $T_{\text{cr}} = 65 \text{ K}$ (HM79) and 35 K are applied. With $T_{\text{cr}} = 65 \text{ K}$, however, the H_2 molecular abundance in the shell is hardly affected in all examined models. With $T_{\text{cr}} = 35 \text{ K}$, the accumulation of H_2 molecules in the shell is slightly delayed, but the shell is finally dominated by H_2 molecules. The H_2 abundance in the shell is reduced only by 2% in model S41 (Paper I) and 5% in model S41-HD at $t \sim 20 t_{\text{dyn}}$. In the region where H_2 molecules accumulate, the FUV radiation is well shielded and the dust temperature is low. Therefore, even if the reformation is inefficient above several ten K, our conclusions do not change.

6.1.3. *Small Grains*

Our calculations do not include detailed energy and ionization balance of the small grains such as polycyclic aromatic hydrocarbons (PAHs). The ionization rate and size distribution of small grains are important factors for the PDR structure. The photoelectric heating rate depends on the abundance and ionization rate of PAHs, and the dust attenuation law of FUV photons may be slightly affected by the change of the grain size distribution. We have calculated some models with different photoelectric heating rates given by Weingartner & Draine (2001) based on the different abundance of small grains. The temperature profile in the PDR would be modified by a factor of less than 2, but this does not affect our conclusions. Some recent observations detect the strong PAH emission around the H II region. This emission sometimes shows the clear ring-like structure, which should trace the shell (e.g., Zavagno et al. 2006). The expected PAH emission related to the time evolution

of the shell will be very useful for these observations, which should be included in future modeling.

6.2. Realistic Structure of Molecular Clouds

The actual molecular clouds have complex structures rather than the homogeneous density distribution assumed in this paper. Below, we briefly discuss how realistic density structures affect the time evolution of the swept-up shell, PDR, as well as the H II region.

6.2.1. Density Gradient

When the H II region forms near the edge of a molecular cloud, or in a cloud with the density gradient (e.g., $n \propto r^{-w}$), its time evolution is different from that in a homogeneous medium. The high-pressure ionized gas is hardly trapped, and flows out of the cloud (Tenorio-Tagle 1979; Franco et al. 1990). Such “blister-like” or “champagne flow” features have been observed in some H II regions. In these regions, only a small fraction of the swept-up gas remains in the shell, and the expanding IF finally destroys the parental molecular cloud. As argued by Whitworth (1979) and Franco et al. (1994), the rapid ionization of the molecular gas will quench the star formation activity in the clouds. Furthermore, we note that the star-forming capacity of the clouds will be limited by FUV photons as well as UV photons. Unless the swept-up gas remains in the shell, stellar FUV radiation is hardly attenuated through the shell. Such unshielded FUV photons dissociate molecules efficiently over a much wider region than the H II region, which reduces the star formation efficiency of the clouds. The dynamical expansion of the H II region, PDR, and the shell in a cloud with a density gradient has not been studied well, and this will be explored in our forthcoming papers.

6.2.2. Clumpiness

Real molecular clouds generally have clumpy or hierarchical structures. The pre-existing density inhomogeneity in molecular clouds can modify the structure and the evolution of the H II region, PDR, and the swept-up shell.

In the H II region, the pre-existing clumps are gradually photoevaporated by stellar UV radiation. These clumps are basically smoothed out in the sound crossing time of each clump, which is much shorter than the dynamical time of the H II region, $t_{\text{dyn}} = R_{\text{st}}/C_{\text{HII}}$.

Outside the H II region, the PDR structure depends on how deep the FUV radiation penetrates into the molecular region. Some previous work (e.g., Boissé 1990) has shown that the radiative transfer in a clumpy medium can be reduced to that of a homogeneous medium with the same average density and lower effective extinction. In the PDR around the H II region, the FUV photons will easily seep into the molecular region, threading the clumpy structure. This will delay the SF and IF overtaking the DFs, and the accumulation of molecules in the shell. In clumpy molecular clouds, on the other hand, most of the gas is thought to be contained in optically thick clumps. Molecules in these opaque clumps will be protected against the FUV radiation by the self-shielding of these clumps. In order to study these two competing effects, multi-dimensional and time-dependent calculations are needed. Note, however, that our 1-D calculation has successfully explained the observed molecular abundance around Sh104 (Paper I). Thus we expect that our 1-D calculations should be a good approximation for the averaged physical quantities.

6.2.3. *Turbulent Velocity Field*

Observation shows that there are the supersonic turbulent motions in molecular clouds (e.g., Elmegreen & Scalo 2004). Since the velocity dispersion increases with the lengthscale (\sim a few km/s at about 10 pc), the effect becomes important with the lower ambient density. The expanding shell actually dissolves when the shell velocity becomes less than the velocity dispersion of the turbulent motion. In §5, we have shown that the shell velocity becomes less than a few km/s when the molecular gas accumulates in the shell with the lower-mass star. In this case, the shell will dissolve without gathering the molecular material, and the triggered star formation will not occur. We study the net feedback effect in the turbulent molecular cloud in a subsequent paper.

6.3. **After the Cloud Destruction**

In this paper, we have considered only the expanding H II region in the molecular cloud, which can trigger the propagation of star formation activity within the cloud. After the molecular cloud disperses due to the negative feedback from massive stars and/or the external turbulent motion, stellar UV photons spread into the diffuse neutral medium. The H II regions expand in the ambient neutral medium, but the SF preceding the IF should also compress the neutral gas to enable the rapid reformation of molecules (e.g., Koyama & Inutsuka 2000; Bergin 2004, and references therein). The role of the giant H II regions expanding in the diffuse neutral medium will be explored in our next paper, Hosokawa &

Inutsuka (2006, in preparation).

7. Conclusions

In this paper, we have studied the time evolution of the H II region, PDR, and the swept-up shell around a massive star, performing the numerical calculation of radiation-hydrodynamics. Following Paper I, we have investigated how the time evolution changes with the different ambient number density and the luminosity (mass) of the central star. The basic evolution with different parameters is qualitatively similar to the fiducial one explained in Paper I, but quantitatively different. We have derived some simple scaling relations, (31)-(35) and (39)-(43), with which we can well understand what causes the differences among models.

First, we have analyzed the dependence on the ambient number density. Our results are summarized as follows:

1. At the typical ambient number density of GMCs, $n_{\text{H},0} = 10^{2-4} \text{ cm}^{-3}$, the molecular gas is finally accumulated in the shell, and gravitational fragmentation is expected.
2. The timescale of the evolution, size of the H II region, and the swept-up mass in the shell quantitatively change with the different ambient number densities. With the lower number density, the H II region expands into the larger region over a long timescale, so that the swept-up mass in the shell is larger. The expected timescale within which the layer becomes gravitationally unstable is also longer with the lower ambient number density.
3. The H_2 molecules rapidly accumulate in the shell, but CO molecules are more sensitive to the shielding effect of FUV photons. With the lower number density, the accumulation of CO molecules in the shell is delayed owing to the small column density of the shell. At $n_{\text{H},0} = 10^4 \text{ cm}^{-3}$, the shell is dominated by CO molecules before the fragmentation. At $n_{\text{H},0} = 10^2 \text{ cm}^{-3}$, however, the shell-fragmentation is expected to take place before the accumulation of CO molecules. If the shell fragments into clumps with high column density, CO molecules will be formed there owing to the self-shielding of clumps.

Next, we have analyzed the dependence on the luminosity (mass) of the central stars. Our results are the following:

4. With the central stars of $M_* = 101 - 12 M_\odot$, the molecular gas is finally accumulated in the shell, and gravitational fragmentation is expected.
5. The timescale of the shell-fragmentation is relatively insensitive to the luminosity of the central star. At $n_{\text{H},0} \sim 10^3 \text{ cm}^{-3}$, the unstable region spreads in the shell over 0.5–2 Myrs with the central star of $M_* = 101 - 12 M_\odot$, whose UV and FUV luminosities differ by 2-4 orders of magnitude.
6. The maximum density of the shell is always higher with the more massive central star. This is due to the difference in the Mach number of the SF. With the higher-mass star, the FUV radiation is easily shielded and the temperature in front of the SF quickly decreases, which raises the Mach number.

According to the above results, we can conclude that an expanding H II region in homogeneous molecular gas should be an efficient trigger for star formation. Once the massive star is ignited in the cloud, the star formation can propagate to the remaining molecular material around the exciting massive star.

We are grateful to Shin Mineshige, Takashi Nakamura, Toru Tsuribe, Kazu Omukai, Hiroshi Koyama, and Akira Mizuta for their useful comments and encouragement. We also owe thanks to the YITP and NAOJ computer systems for the numerical calculations. SI is supported by the Grant-in-Aid (15740118, 16077202) from the Ministry of Education, Culture, Sports, Science, and Technology (MEXT) of Japan.

A. Finite Difference Method

In this section, we explain the difference method for the ionization equation and the energy equation, (27). Other rate equations are differenced in the same way as the ionization equation. For simplicity, we temporarily omit all indices and drop the frequency-dependence of the radiation field in the ionization equation,

$$\frac{dX}{dt} = (1 - X)\sigma F + R, \quad (\text{A1})$$

where R means some processes other than photoionization (e.g., recombination etc). The simplest difference form of (A1) is,

$$\frac{X_j^{n+1} - X_j^n}{\Delta t} = \sigma \{(1 - X_j)F_j\}^{n+1/2} + R_j^{n+1/2}, \quad (\text{A2})$$

where all physical quantities are defined at the cell center. The time average, $Q_j^{n+1/2}$ for a quantity, Q is defined as

$$Q_j^{n+1/2} = \frac{Q_j^{n+1} + Q_j^n}{2}. \quad (\text{A3})$$

Using the radiative transfer equation, (8), the UV photon number flux in the j -th cell, F_j is written in time steps,

$$F_j = F_{j-1} \frac{r_{j-1}^2}{r_j^2} \exp\left(-\sigma \int_{r_{j-1}}^{r_{j+1}} n(1 - X) dr\right). \quad (\text{A4})$$

Eliminating F_j^{n+1} in equation (A2) with (A4), we can calculate X_j^{n+1} iteratively with other rate equations and the energy equation. However, this differenced form provides no reliable results. If the optical depth through the j -th cell is thick enough, $\Delta\tau_j \gg 1$, the UV flux at the j -th cell center, F_j , significantly decreases from the UV flux at the previous cell center, F_{j-1} . Even if a sufficient number of UV photons reaches the cell interface at $r_{j-1/2}$, only a few photons may reach the j -th cell center and the j -th cell will not be photoionized. This situation occurs at the ionization front (IF), where the optical depth changes sharply.

The quick way to improve the scheme is to define the flux at the inner cell interface, not in the cell center. However, we adopt another more sophisticated differenced form for rate equations. With equation (A1) and radiative transfer equation (7), the ionization equation becomes,

$$\frac{dX}{dt} = -\frac{1}{nr^2} \frac{\partial(r^2 F)}{\partial r} + R. \quad (\text{A5})$$

First, equation (A5) is differenced for the spatial grids,

$$\frac{dX_j}{dt} = \frac{r_{j-1/2}^2 F_{j-1/2} [1 - \exp(-n_j \sigma (1 - X_j) \Delta r_j)]}{n_j (r_{j+1/2}^3 - r_{j-1/2}^3) / 3} + R_j. \quad (\text{A6})$$

In the right-hand side, the first term represents the consumption rate of UV photons for the photoionization per unit volume. This equation assures that the number of ionized atoms per unit time is equal to that of the consumed photons per unit time in the j -th cell, if other processes, R_j , are neglected.

Since the ionization rate sharply changes at the IF, X_j should be calculated with some precision (e.g, Mathews 1965; Tenorio-Tagle 1976). We approximate the time evolution of the ionization rate between two time steps with the power-law form,

$$X_j(t) = X_j^n + \frac{X_j^{n+1} - X_j^n}{\Delta t} t, \quad (0 \leq t \leq \Delta t) \quad (\text{A7})$$

and analytically integrate (A6) by time, t from t^n to t^{n+1} . Other terms are calculated in the same manner. With the frequency-dependence of the radiation field and the dust extinction, we can derive the differenced form in a similar way. We use the same differenced form to calculate the photodissociation rate of H_2 and CO molecules. The self-shielding effect works with the low column density ; $N_{\text{H}_2} > 10^{14} \text{ cm}^{-2}$ for H_2 molecules (Draine & Bertoldi 1996) and $N_{\text{CO}} > 10^{15} \text{ cm}^{-2}$ for CO molecules (Lee et al. 1996). The column density of one cell can be much higher than these values in our time-dependent calculations, and we do not use the shielding function given by Draine & Bertoldi (1996) and Lee et al. (1996).

The energy equation (27) is differenced as,

$$\begin{aligned} \frac{T_j^{n+1} - T_j^n}{\Delta t} &+ \left(\frac{T}{2w}\right)^{n+1/2} \left(\frac{X_{\text{H},j}^{n+1} - X_{\text{H},j}^n}{\Delta t} + 3\frac{X_{\text{H}^+,j}^{n+1} - X_{\text{H}^+,j}^n}{\Delta t}\right) \\ &+ \frac{\mu m_{\text{H}}(\gamma - 1)}{k} \left\{ \left(\frac{u}{w}\right)^{n+1/2} r^2 \frac{\partial p}{\partial m} - \left(\frac{1}{w}\right)^{n+1/2} \frac{\partial(r^2 u p)}{\partial m} - \left(\frac{1}{w}\right)^{n+1/2} \frac{\partial(r^2 q_{\text{cond}})}{\partial m} \right\} \\ &= \frac{\gamma - 1}{k} \left(\frac{\Gamma - \Lambda}{w}\right)^{n+1/2}. \end{aligned} \quad (\text{A8})$$

With differenced ionization equation (A6), other similar rate equations, and the energy equation (A8), we iteratively solve the new temperature, T_j^{n+1} and chemical compositions, $X_{s,j}^{n+1}$.

B. Necessity of Thermal Conduction – Field Condition –

We include the heat transfer by thermal conduction in the energy equation (3). Recently, Koyama & Inutsuka (2004) have shown that the thermal conduction must be included to calculate the gas-dynamics with the thermal instability (TI). The conduction stabilizes the

TI for the short wavelength and the critical wavelength is called the Field length,

$$\lambda_F = \left(\frac{KT}{n\Lambda} \right)^{1/2}, \quad (\text{B1})$$

(Field 1965) where K is the conductivity and Λ is the cooling rate per hydrogen atom. Koyama & Inutsuka (2004) have shown that the Field length must be resolved with several spatial cells to converge the calculation, increasing the number of spatial grids. In our calculations, the TI occurs around $T \sim \text{several} \times 10^3$ K mainly at the IF. If we do not include the thermal conduction, unphysical oscillation spreads from the IF and the calculation does not converge. Therefore, we need to include the thermal conduction in the energy equation.

Since the Field length is generally much shorter than the characteristic length scale (e.g., Strömgren radius) in our calculations, we adopt another available method to resolve Field length. We first determine the width of the cell, Δr_j and calculate the conductivity, K_j so that the Field length is longer than the given width of the cell. The index j means the difference step in space. If we set $\lambda_F \sim 3\Delta r_j$, such conductivity is calculated as,

$$K_j = \frac{9n_j\Lambda_j}{T_j} (\Delta r_j)^2. \quad (\text{B2})$$

The conductivity, K_j is calculated every time step with equation (B2). If we set 100 cells per initial Strömgren radius for the ambient number density, 10^3 cm^{-3} , the calculated conductivity is, $K \sim 4 \times 10^{11-10} \text{ erg cm}^{-1} \text{ K}^{-1} \text{ s}^{-1}$, which is significantly larger than the standard value. However, the conduction with equation (B2) smooths out the temperature structure only on the Field length scale, which covers a few cells ($\lambda_F \sim 3\Delta r_j$). Since the meaningful temperature profile changes over a much longer length scale, we use the equation (B2) to calculate the conductivity.

C. Doppler Shift of Lines

C.1. Doppler Effect for Cooling Lines

The dominant cooling processes in the PDR are the radiative loss by the fine-structure transitions, [OI] $63.1 \mu\text{m}$ and [CII] $157.7 \mu\text{m}$ (Hollenbach & Tielens 1999). These lines can be optically thick at $N_{\text{H}} > 10^{21} \text{ cm}^{-2}$ (Hollenbach & McKee 1979, 1989), and we use the escape probability for these lines (de Jong et al. 1980; Tielens & Hollenbach 1985). Since the swept-up shell expands at a supersonic velocity relative to the ambient gas, a few - 10 km/s, we take account of the Doppler shift for the trapping effect. The gas velocity in the shell is usually almost constant, and we separately calculate the escape probability for the gas in

the shell and ahead of the shell. For the gas in the shell, photons can escape from the inner (IF) and outer edge (SF) of the shell,

$$\beta_{\text{esc}} = f_{\text{esc}}(\tau_{x,\text{s1}}) + f_{\text{esc}}(\tau_{x,\text{s2}}), \quad (\text{C1})$$

where β_{esc} is the escape probability, $\tau_{x,\text{s1}}$ and $\tau_{x,\text{s2}}$ are the optical depth averaged over the line to the IF and the SF respectively, and $f_{\text{esc}}(\tau)$ is defined as,

$$\begin{aligned} f_{\text{esc}}(\tau) &= \frac{1 - \exp(-2.34\tau)}{4.68\tau} & \tau < 7, \\ &= \left\{ 4\tau \left[\ln \left(\frac{\tau}{\sqrt{\pi}} \right) \right]^{0.5} \right\}^{-1} & \tau \geq 7 \end{aligned} \quad (\text{C2})$$

(de Jong et al. 1980). For the gas ahead of the shell, we assume that only half of the photons can escape from the SF,

$$\beta_{\text{esc}} = f_{\text{esc}}(\tau_{x,\text{ad}}), \quad (\text{C3})$$

where $\tau_{x,\text{ad}}$ is the optical depth to the SF. The CO molecules are another important coolant in the PDR. We do not solve the non-LTE rotational level population, to save the computational time, but adopt the analytical formulae given by Hollenbach & McKee (1979) including the trapping effect. We take account of the Doppler shift for the trapping effect in the same manner as the fine-structure lines. In our calculations, the rovibrational lines of H₂ molecules are reliably optically thin.

C.2. Doppler Effect for Photodissociating Lines

The FUV photons emitted from the central star photodissociate the molecules, both in the swept-up shell and in the unshocked ambient medium. However, we do not include the Doppler effect for the photodissociating lines of H₂ and CO molecules. Below, we briefly verify this approximation. The Doppler shift in the FUV energy range is, $h\Delta\nu_{\text{d}} = h\nu_0(u_{\text{sl}}/c) \sim 10^{-4}$ eV, where $h\nu_0 \sim 10$ eV is the characteristic energy of FUV photons, $u_{\text{sl}} \sim 10$ km/s is the typical velocity of the shell, and c is the speed of light. The Doppler shift is larger than the Doppler width of lines owing to the supersonic velocity of the shell. As noted in §2.1, however, the absorption of FUV photons in the Doppler core is not important. In our calculations, for example, the column density of H₂ molecules easily exceeds $N_{\text{H}_2} \sim 10^{19}$ cm⁻², and the FUV photons are mainly absorbed in the Lorentz wings after that. Since the energy range of the Lorentz wings is much wider than that of the Doppler core, the Doppler shift of the core is not so important.

REFERENCES

- Abgrall, H., Le Bourlot, J., Pineau des Forets, G., Roueff, E., Flower, E.R. & Heck, L. 1992, A&A, 253, 525
- Abgrall, H., Roueff, E., Launay, F., Roncin, J.Y. & Subtil, J.L. 1993, A&AS, 101, 273
- Allison, A.C. & Dalgarno, A. 1970, At. Data. 1, 289
- Arthur, S.J., Kurtz, S.E., Franco, J. & Albarran, Y. 2004, ApJ, 608, 282
- Bakes, E.L.O & Tielens, A.G.G.M. 1994, ApJ, 427, 822
- Bergin, E.A., Hartmann, L.W., Raymond, J.C. & Ballesteros-Paredes, J. 2004, ApJ, 612, 921
- Bertoldi, F. 1989, ApJ, 346, 735
- Bertoldi, F. & Draine, B.T. 1996, ApJ, 458, 222
- Bertoldi, F. & McKee, C.F. 1990, 354, 529
- Black, J.H. & Dalgarno, A. 1977, ApJS, 34, 405
- Blitz, L. & Shu, F.H. 1980, ApJ, 238, 148
- Boissé, P., 1990, A&A, 228, 483
- Cazaux, S. & Tielens, A.G.G.M. 2002, ApJ, 575, L29
- Cazaux, S. & Tielens, A.G.G.M. 2004, ApJ, 604, 222
- Churchwell, E. 2002, ARA&A, 40, 27
- de Jong, T., Dalgarno, A. & Boland, W. 1980, ApJ, 91, 68
- Deharveng, L. et al. 2003, A&A, 408, 25L
- Deharveng, L., Zavagno, A. & Caplan, J. 2005, A&A, 433, 565
- Diaz-Miller, R.I., Franco, J. & Shore, S.N. 1998, ApJ, 501, 192
- Draine, B.T. & Bertoldi, F. 1996, ApJ, 468, 269
- Elmegreen, B.G. & Lada, C.J. 1977, ApJ, 214, 725
- Elmegreen, B.G. 1989, ApJ, 340, 786

- Elmegreen, B.G. & Scalo, J. 2004, *ARA&A*, 42, 211
- Field, G.B. 1965, *ApJ*, 142, 531
- Franco, J., Tenorio-Tagle, G. & Bodenheimer, P. 1990, *ApJ*, 349, 12
- Franco, J. & Shore, S.N. 1984, *ApJ*, 285, 813
- Franco, J., Shore, S.N. & Tenorio-Tagle, G. 1994, *ApJ*, 436, 795
- Galli, D. & Palla, F. 1998, *A&A*, 335, 403
- Garcia-Segura, G. & Franco, J. 1996, *ApJ*, 469, 171
- Habing, H.J. 1968, *Bull. Astron. Inst. Netherlands*, 19, 421
- Hill, J. K. & Hollenbach, D. 1978, *ApJ*, 225, 390
- Hollenbach, D. & Salpeter, E.E. 1970, *J. Chem. Phys.* 53, 79
- Hollenbach, D. & Salpeter, E.E. 1971, *ApJ*, 163, 155
- Hollenbach, D., Werner, M.W. & Salpeter, E.E. 1971, *ApJ*, 163, 165
- Hollenbach, D. & McKee, C.F. 1979, *ApJS*, 41, 555
- Hollenbach, D. & McKee, C.F. 1989, *ApJ*, 342, 306
- Hollenbach, D., Takahashi, T. & Tielens, A.G.G.M. 1991, *ApJ*, 377, 192
- Hollenbach, D., & Tielens, A. G. G. M. 1999, *Rev. Mod. Phys.*, 71, 173
- Hosokawa, T. & Inutsuka, S. 2005, *ApJ*, 623, 917 (Paper I)
- Koyama, H. & Inutsuka, S. 2000, *ApJ*, 532, 980
- Koyama, H. & Inutsuka, S. 2004, *ApJ*, 602, 25L
- Kurucz, R.L. 1993, Kurucz CD-ROM 13 (Cambridge: Smithsonian Astrophysical Observatory)
- Lanz, T. & Hubeny, I. 2003, *ApJS*, 146, 417
- Larson, R.B. 1981, *MNRAS*, 194, 809
- Lee, H.H., Herbst, E., Pineau des Forêts, G., Roueff, E. & Le Bourlot, J. 1996, *A&A*, 311, 690

- Martins, F., Schaerer, D. & Hiller, D.J. 2005, A&A, 436, 1049
- Mathews, W.G. 1965, ApJ, 142, 1120
- Mihalas, D. & Mihalas, B. W. 1984, *Foundations of Radiation Hydrodynamics* (New York: Oxford Univ. Press)
- Nelson, R.P. & Langer, W.D. 1997, ApJ, 482, 796
- Petrosian, V., Silk, J. & Field, G.B. 1972, ApJ, 177, L69
- Roberge, W.G., Jones, D., Lepp, S., & Dalgarno, A. 1991, ApJS, 77, 287
- Roger, R.S. & Dewdney, P.E. 1992, ApJ, 385, 536
- Shull, J.M., 1978, ApJ, 219, 877
- Shull, J.M. & van Steenberg, M.E. 1985, ApJ, 298, 268
- Spitzer, L. 1978, *Physical Processes in the Interstellar Medium* (New York: Wiley).
- Stecher, T.P. & Williams, D.A. 1967, ApJ, 149, L29
- Tenorio-Tagle, G. 1976, A&A, 53, 411
- Tenorio-Tagle, G. 1979, A&A, 71, 59
- Tielens, A.G.G.M. & Hollenbach, D. 1985, ApJ, 291, 722
- van Dishoeck, E.F. & Black, J.H. 1988, ApJ, 334, 771
- van Leer, B. 1979, J.Comput.Phys., 32, 101
- Weingartner, J.C. & Draine, B.T. 2001, ApJ, 548, 296
- Whitworth, A. 1979, MNRAS, 186, 59
- Williams, J.P. & McKee, C.F. 1997, ApJ, 476, 166
- Wolfire, M.G., Hollenbach, D., McKee, C.F., Tielens, A.G.G.M. & Bakes, E.L.O. 1995, ApJ, 443, 152
- Zavagno, A., Deharveng, D., Comeron, F., Brand, J., Massi, F., Caplan, J. & Russeil, D. 2006, A&A, 446, 171

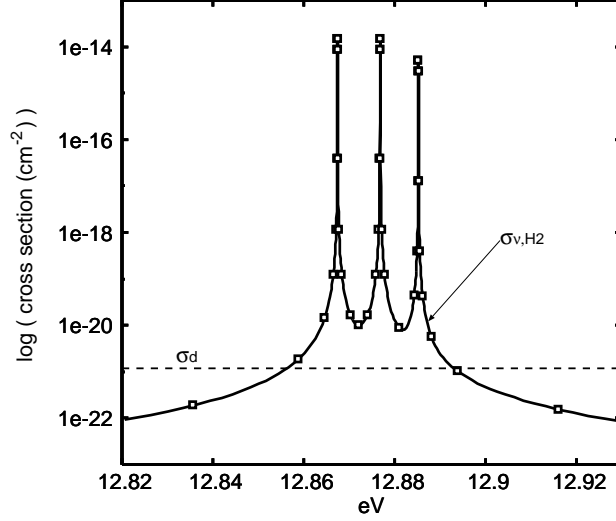


Fig. 1.— Our representative lines for Lyman-bands, σ_{ν,H_2} . The points indicate the center of the grids. The dashed line means the dust absorption cross section for H_2 dissociating FUV photons, σ_{d}

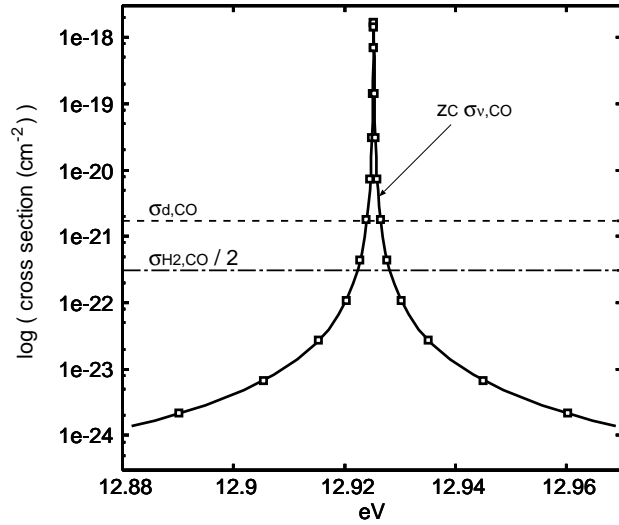


Fig. 2.— Our representative line for the photodissociation of CO molecules, $Z_C \sigma_{\nu,\text{CO}}$. The points indicate the center of the grids. The dashed line (dot-dashed line) means the cross section for the dust absorption (shielding by H_2 molecules), $\sigma_{\text{d,CO}}$ ($\sigma_{\text{H}_2,\text{CO}}/2$).

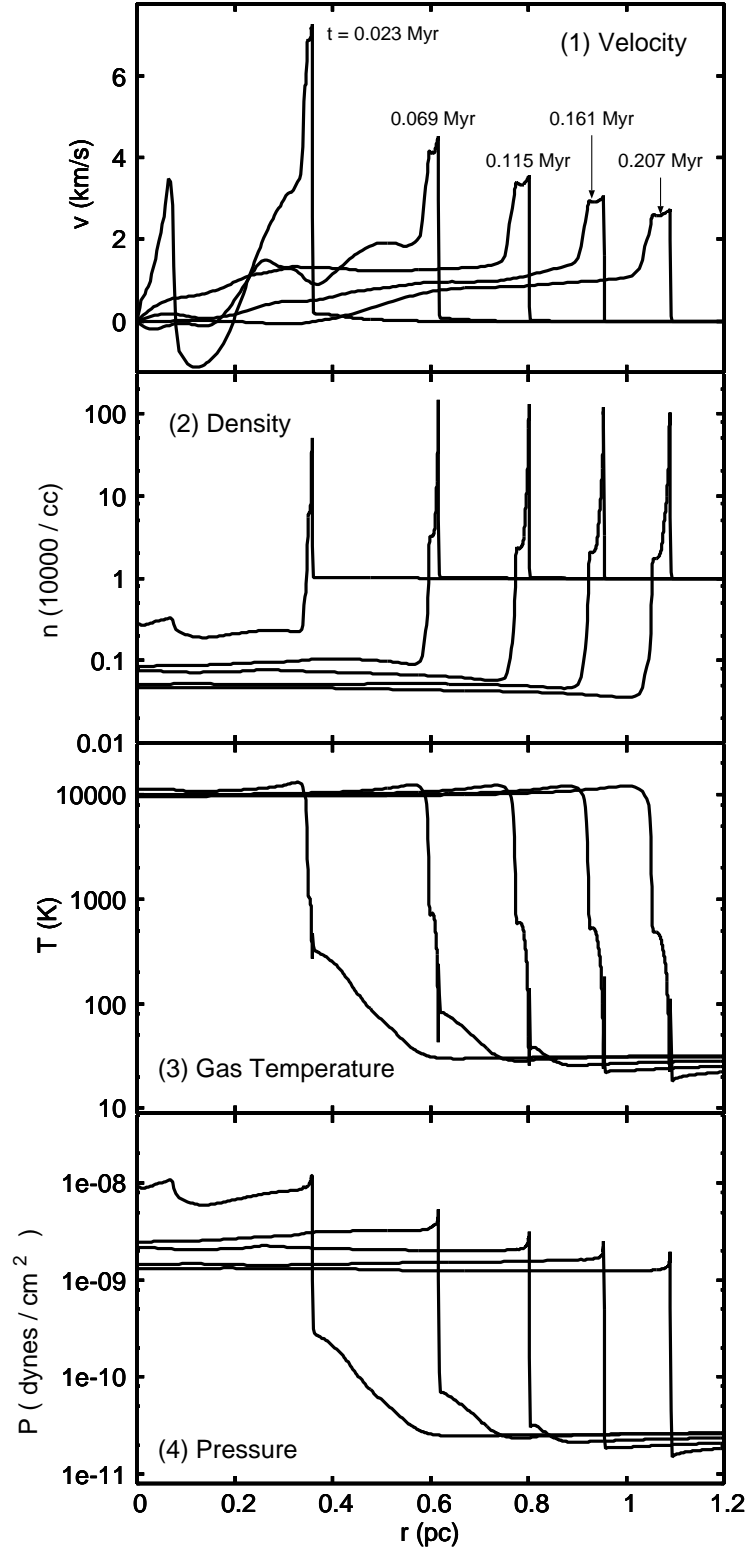


Fig. 3.— The snapshots of the gas-dynamical evolution of model HD-S41. In each panel, five snapshots represent the profiles at $t = 0.023, 0.069, 0.115, 0.161$ and 0.207 Myr respectively.

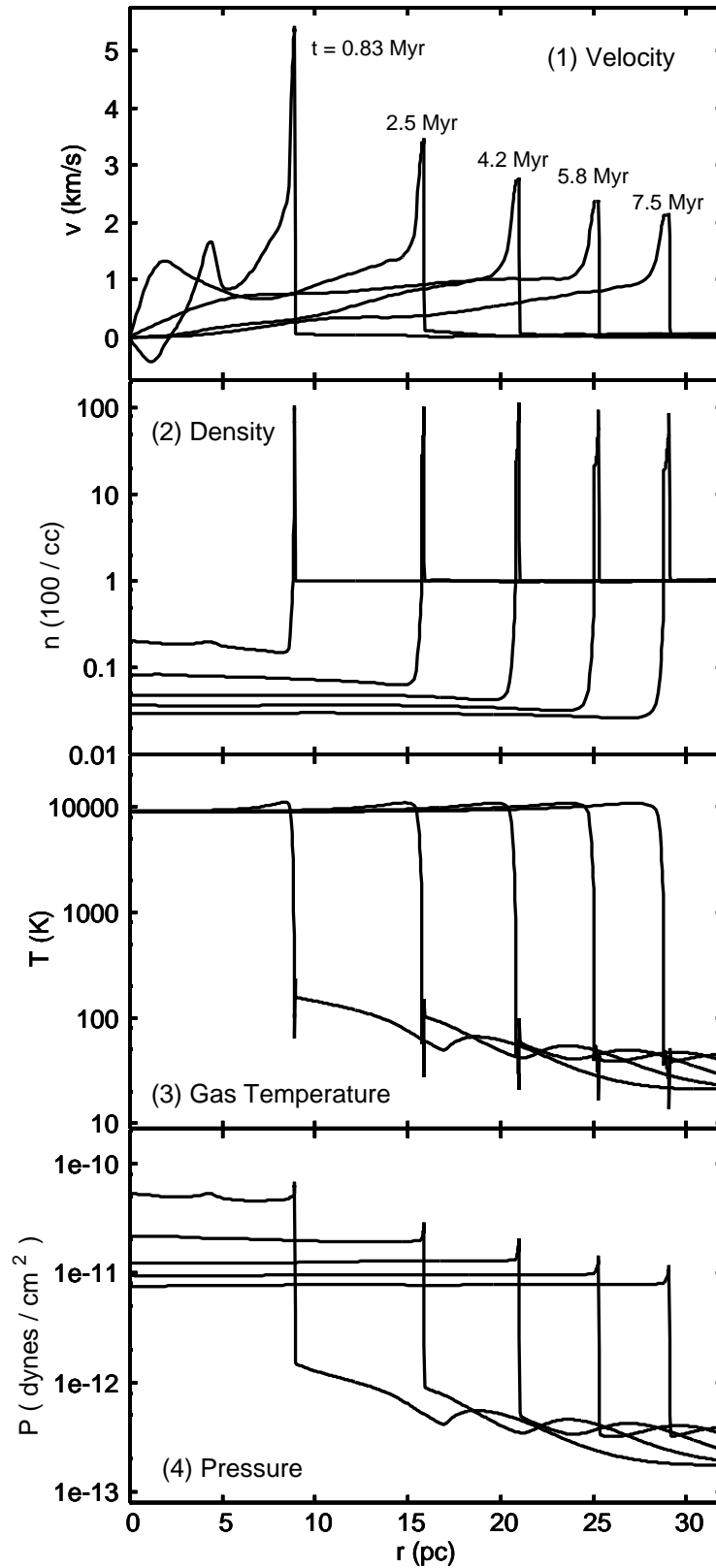


Fig. 4.— Same as Fig3 but for model LD-S41. In each panel, five snapshots represent the profiles at $t = 0.83, 2.5, 4.2, 5.8$ and 7.5 Myr respectively.

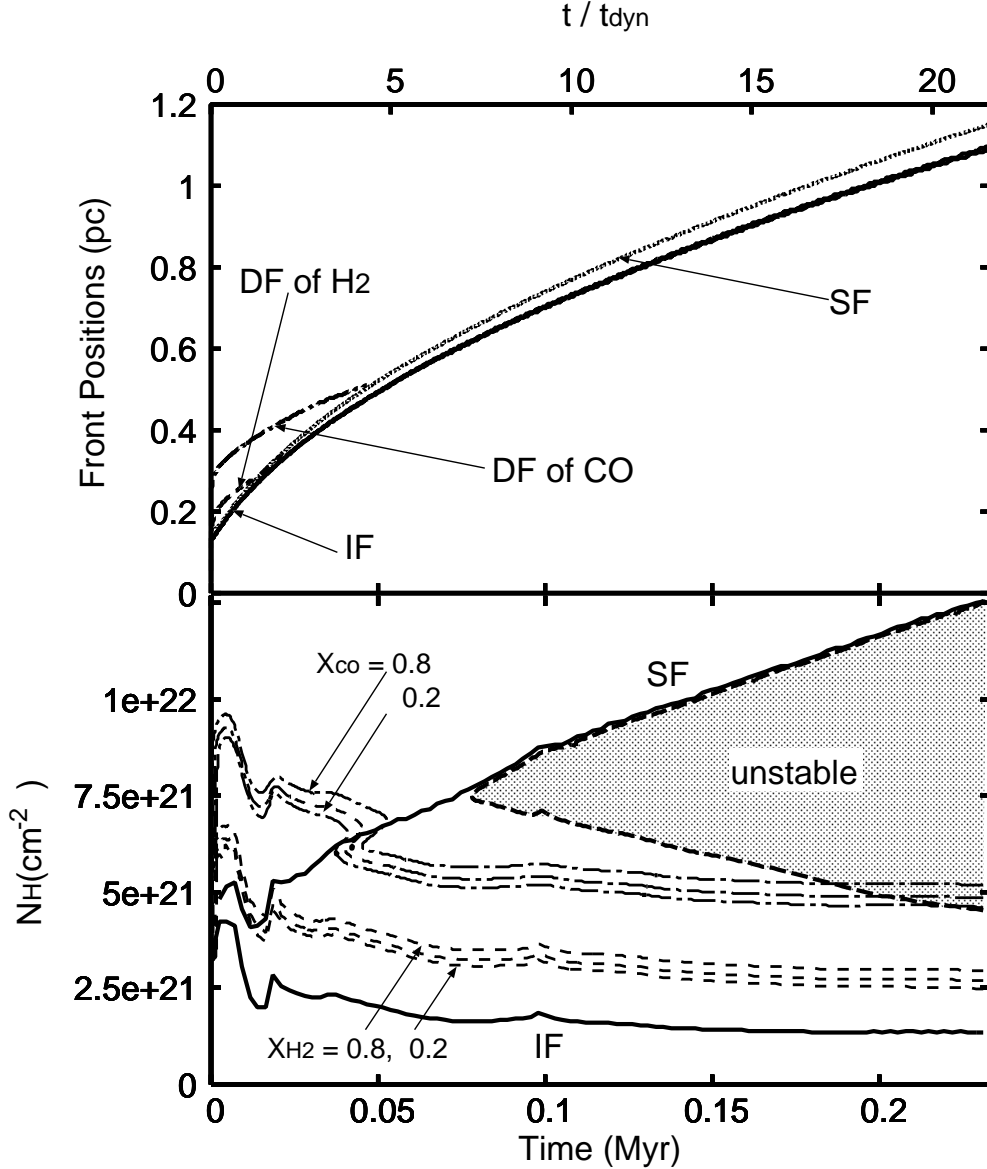


Fig. 5.— *Upper panel:* The time evolution of the various front positions in model HD-S41. The solid and dotted line mean the position of the IF and SF. The broken (dot-solid) line represents the DF of H₂ (CO), where $X_{\text{H}_2} \equiv 2n_{\text{H}_2}/n_{\text{H}_{\text{nuc}}} = 0.5$ and $X_{\text{CO}} \equiv n_{\text{CO}}/n_{\text{C}_{\text{nuc}}} = 0.5$. We plot the position of DFs only before the SF catches up with each DFs. After the DFs are taken in the shell, the positions of DFs are close to that of the SF. *Lower panel:* The time evolution of the column density of each region in model HD-S41, where the vertical axis, N_{H} is the column density of the hydrogen nuclei included in all species of H⁺, H and H₂ from the central star. Thin contour lines represent the position where X_{H_2} (*dashed contours*) and X_{CO} (*dot-dashed contours*) = 0.2, 0.5, and 0.8. The shaded region corresponds to the expected unstable region, where $t > (G\rho)^{-1/2}$.

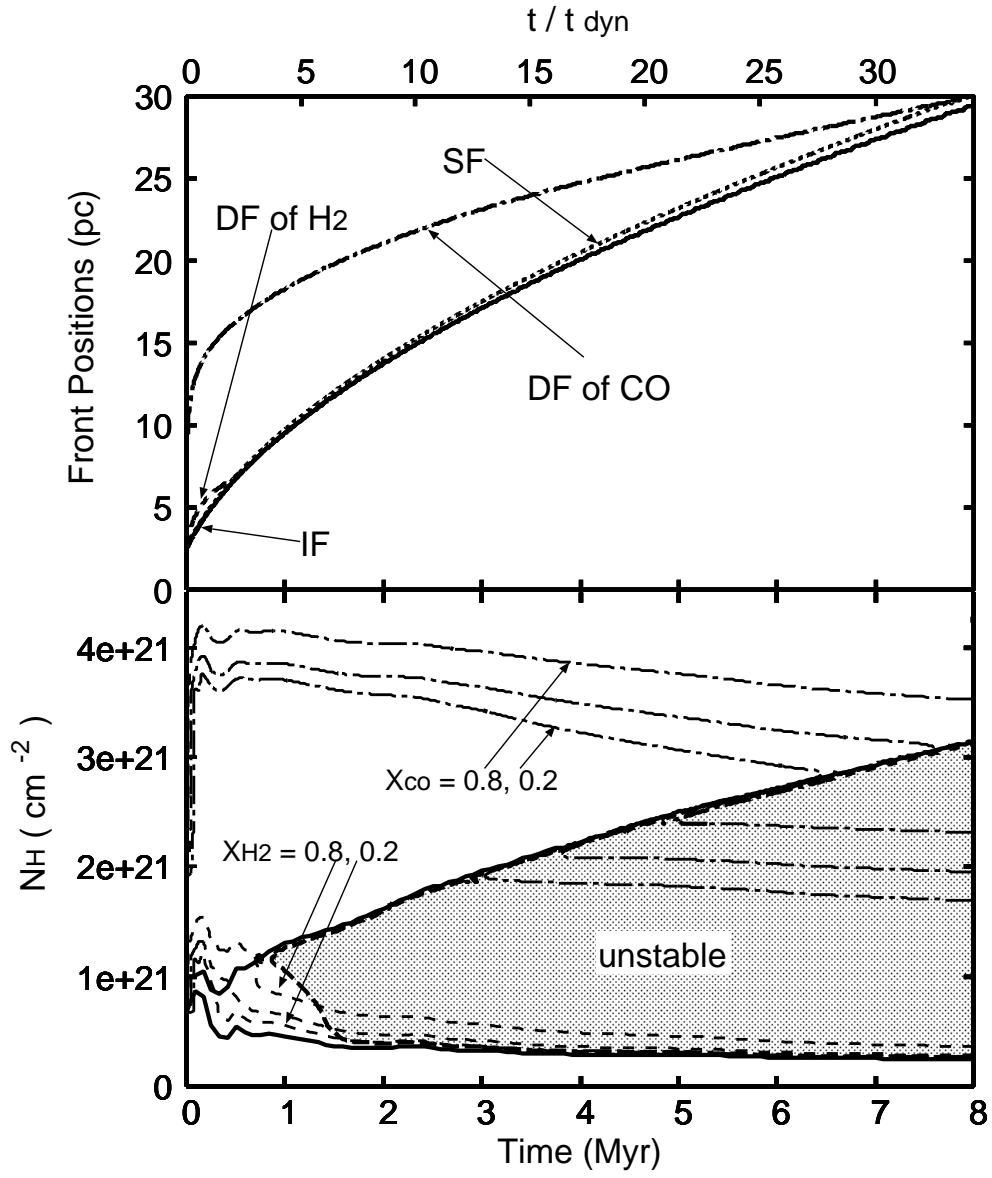
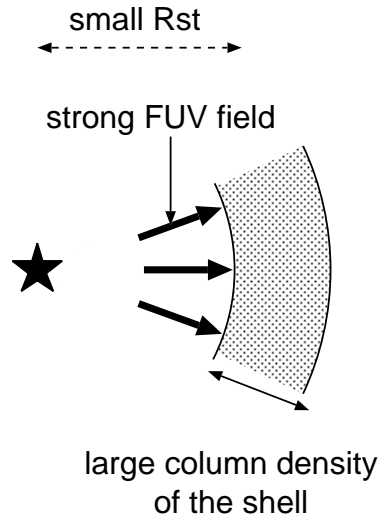


Fig. 6.— Same as Fig.5 but for model LD-S41.

(1) High density case



(2) Low density case

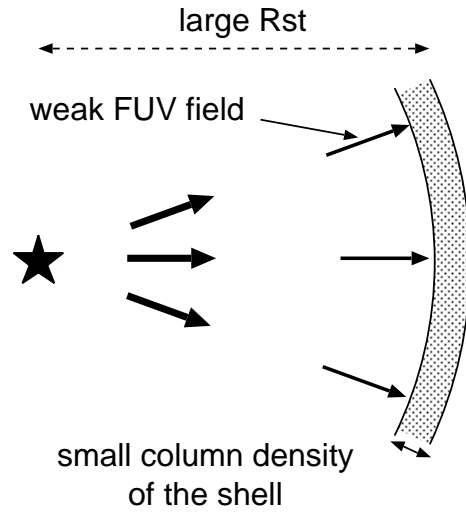


Fig. 7.— Schematic figures for the H II region and the swept-up shell in models with different ambient number densities. These figures show the snapshot at one t/t_{dyn} in both models.

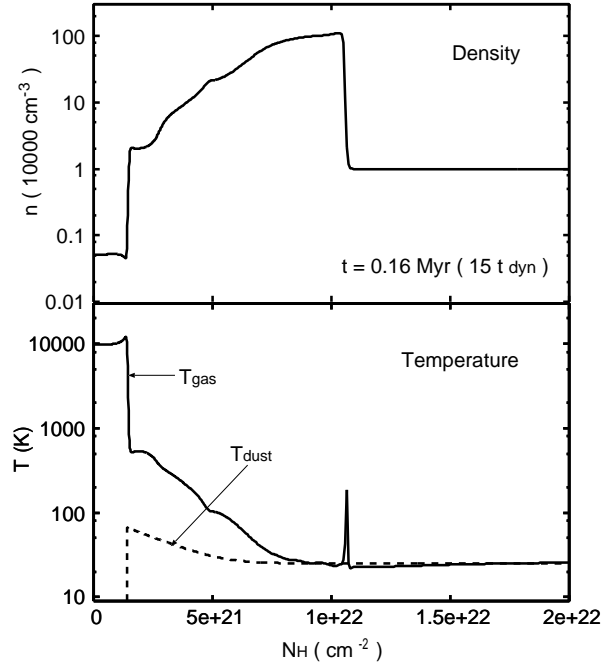


Fig. 8.— The density and the gas/dust temperature profiles in model HD-S41. These snapshots are at $t = 0.161 \text{ Myr}$, which corresponds to $\sim 15 t_{\text{dyn}}$.

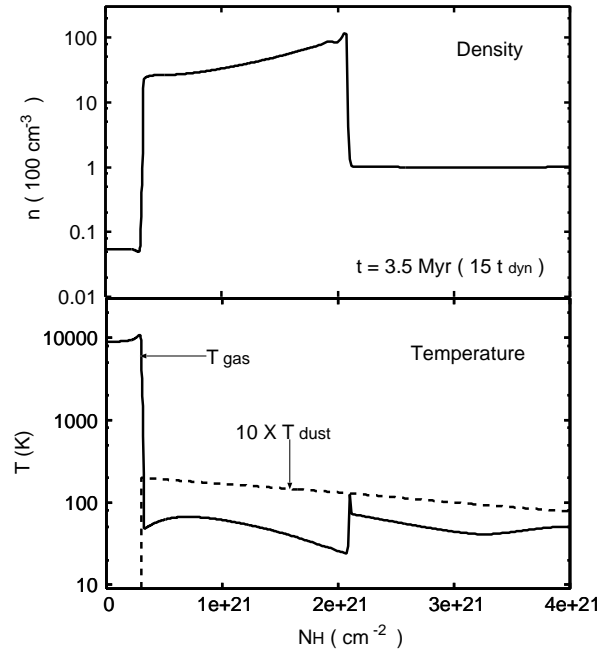


Fig. 9.— Same as Fig.8 but for model LD-S41. These snapshots are at $t = 3.5 \text{ Myr}$, which corresponds to $\sim 15 t_{\text{dyn}}$.

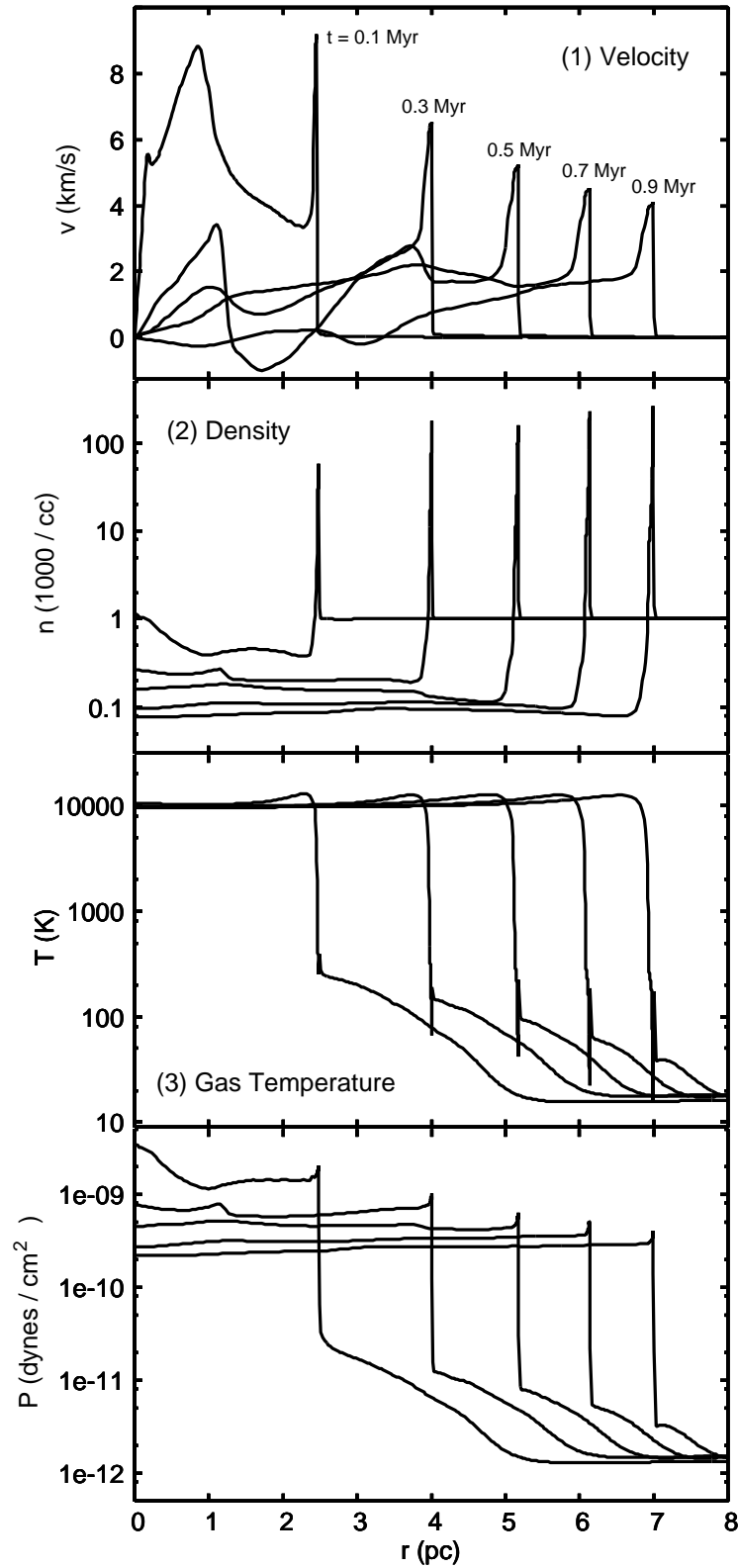


Fig. 10.— Same as Fig3 but for model S101. In each panel, five snapshots represent the profiles at $t = 0.1, 0.3, 0.5, 0.7$ and 0.9 Myr respectively.

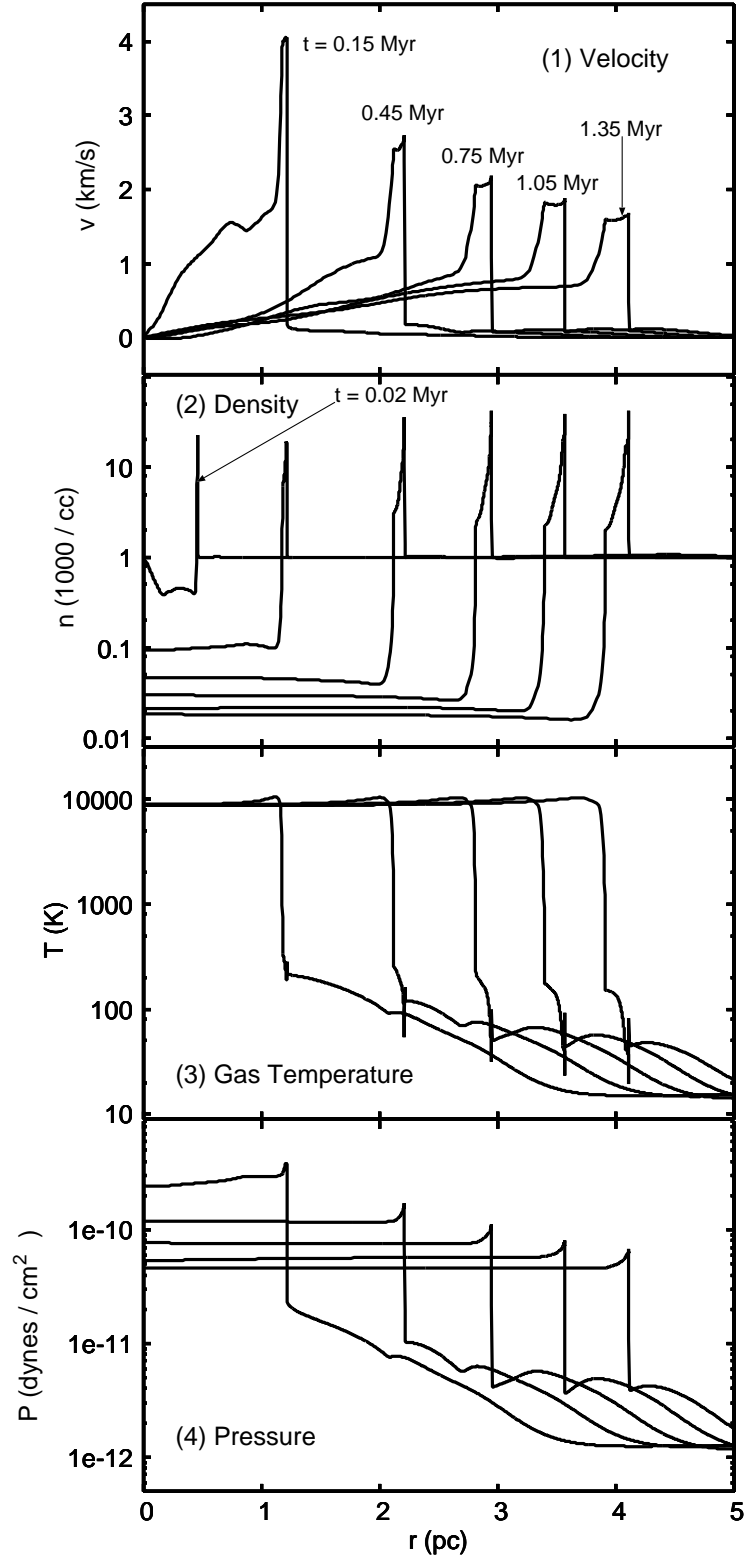


Fig. 11.— Same as Fig3 but for model S19. In each panel, five snapshots represent the profiles at $t = 0.15, 0.45, 0.75, 1.05$ and 1.35 Myr respectively. We add one early snapshot of the density profile at $t = 0.02$ Myr.

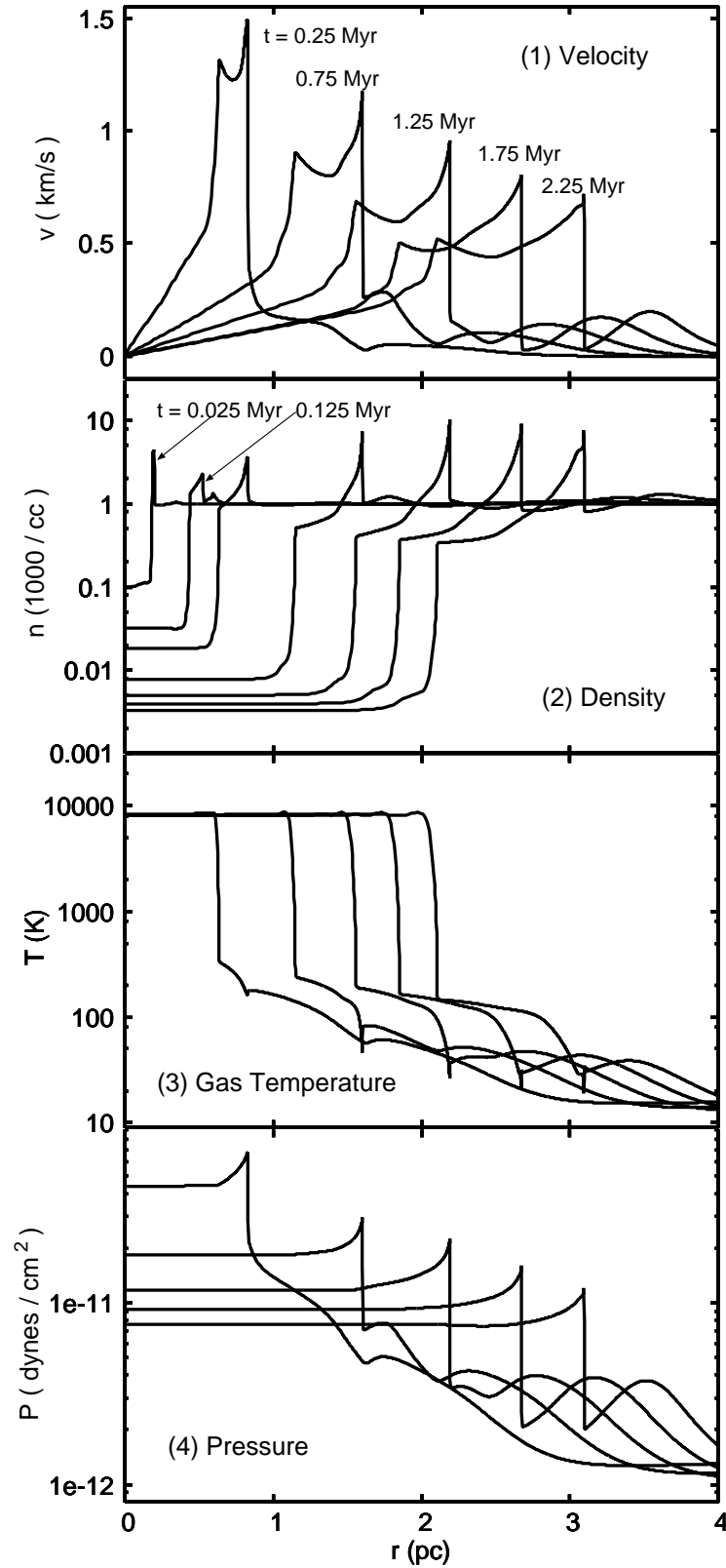


Fig. 12.— Same as Fig3 but for model S12. In each panel, five snapshots represent the profiles at $t = 0.25, 0.75, 1.25, 1.75$ and 2.25 Myr respectively. We add two early snapshots of the density profile at $t = 0.025$, and 0.125 Myr.

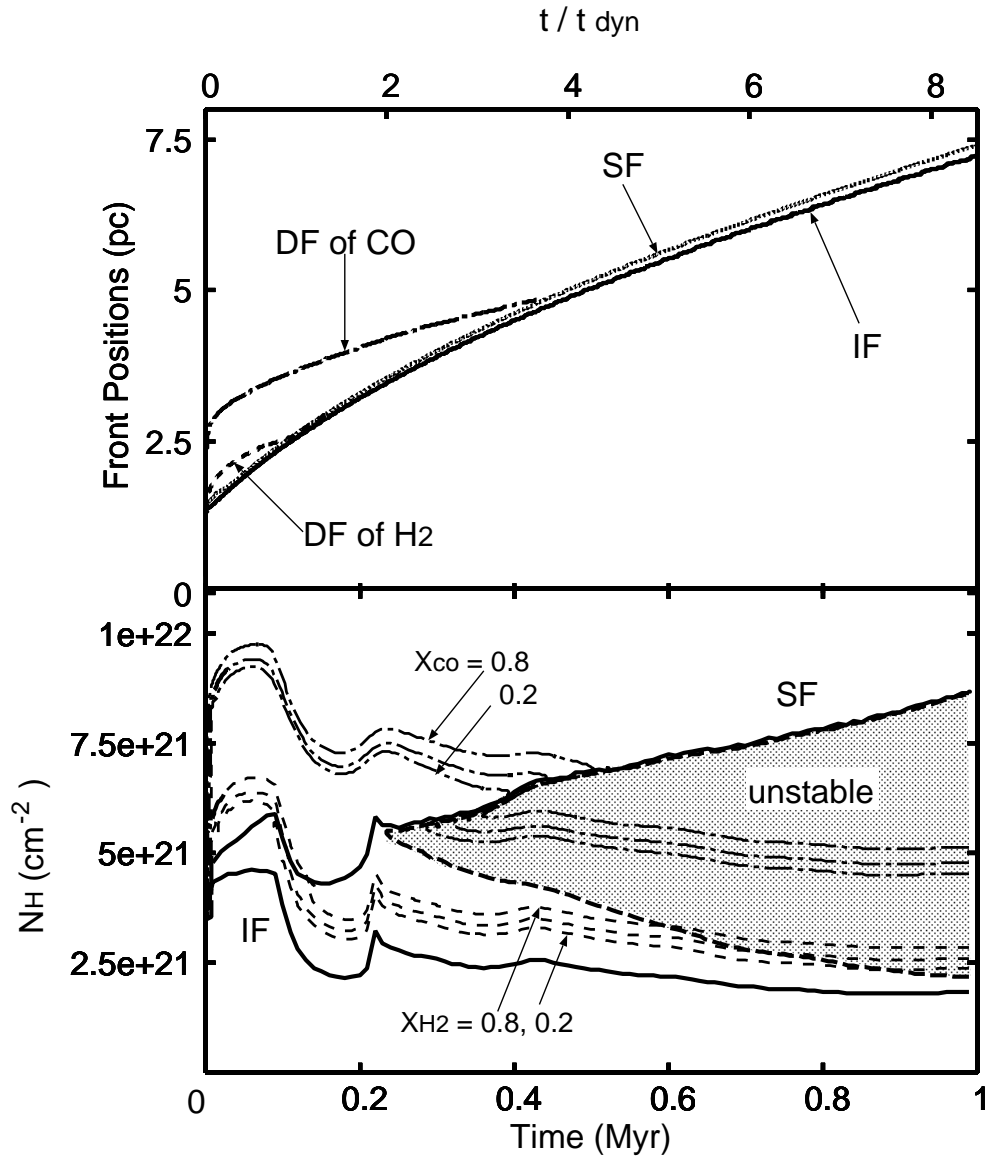


Fig. 13.— Same as Fig.5 but for model S101.

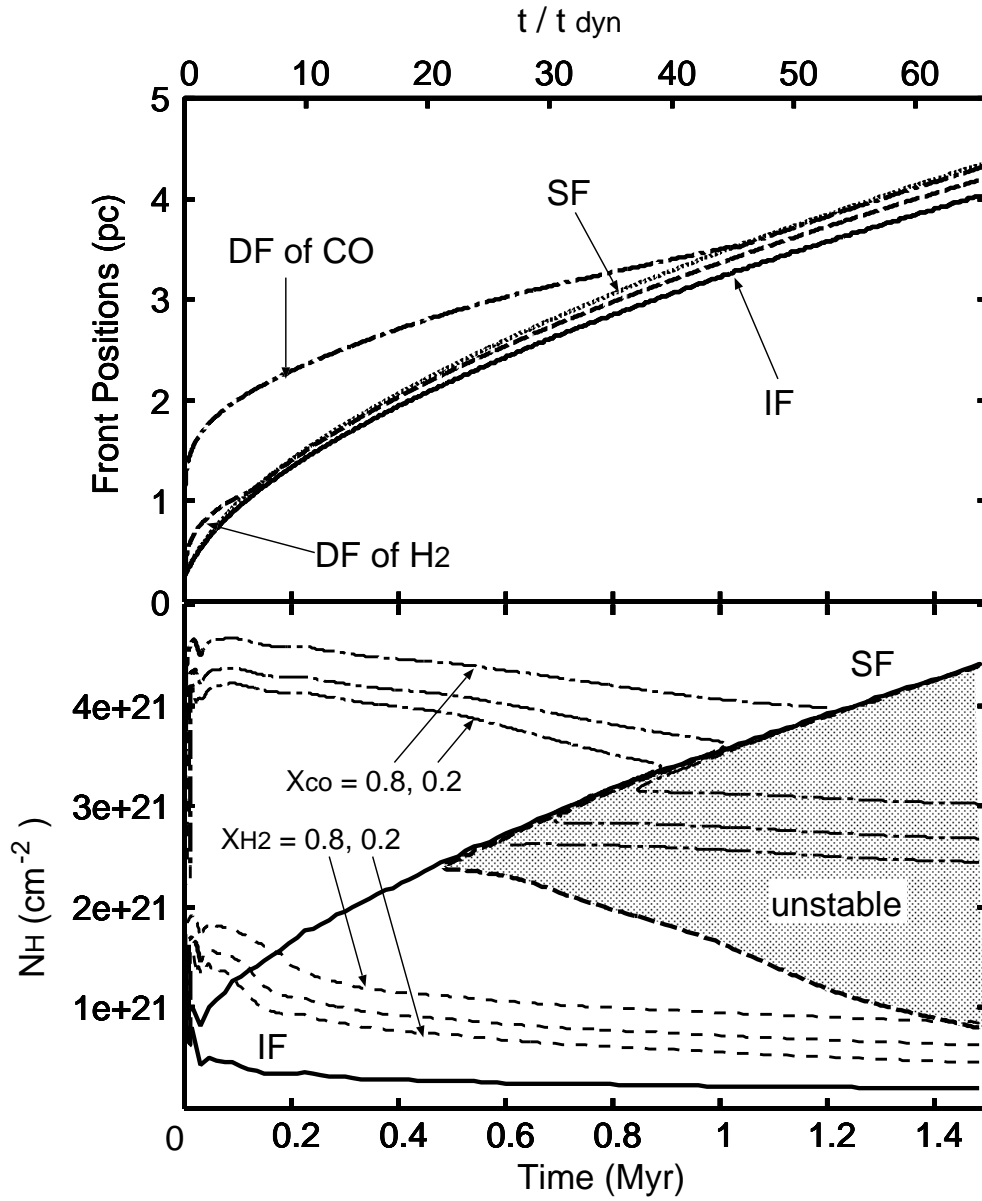


Fig. 14.— Same as Fig.5 but for model S19.

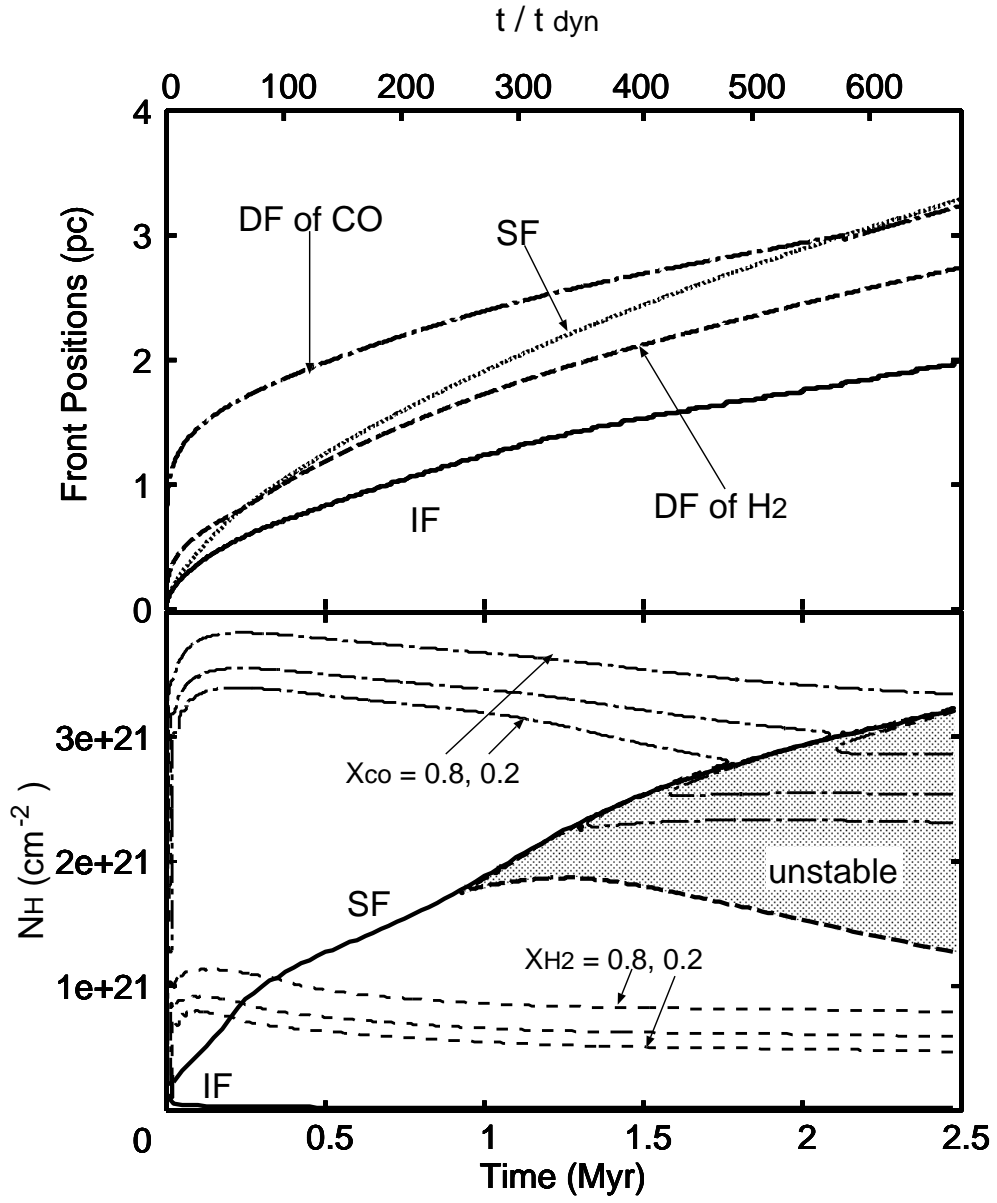


Fig. 15.— Same as Fig.5 but for model S12.

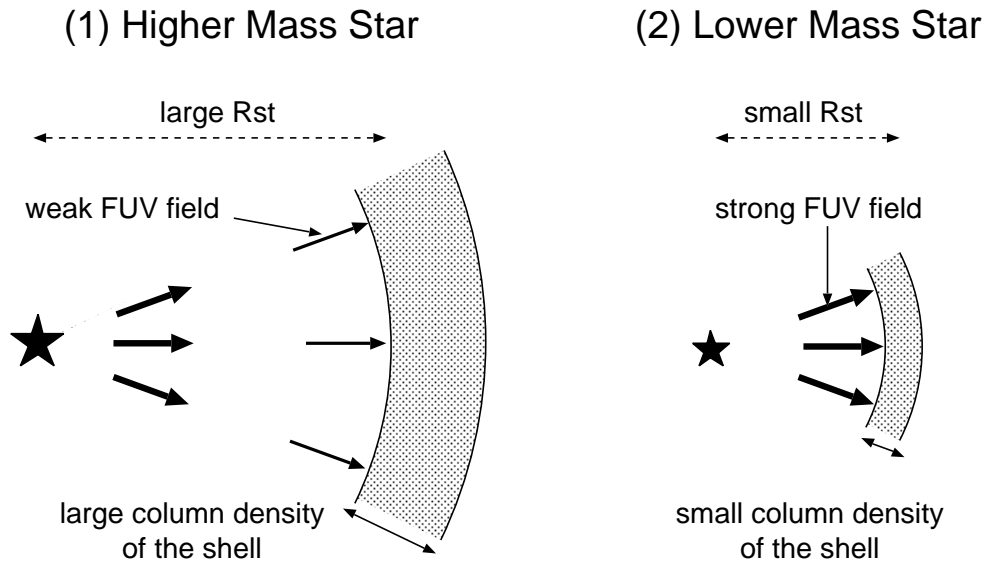


Fig. 16.— Schematic figures for the H II region and the swept-up shell in models with different central stars. These figures show the snapshot at one t/t_{dyn} in both models.

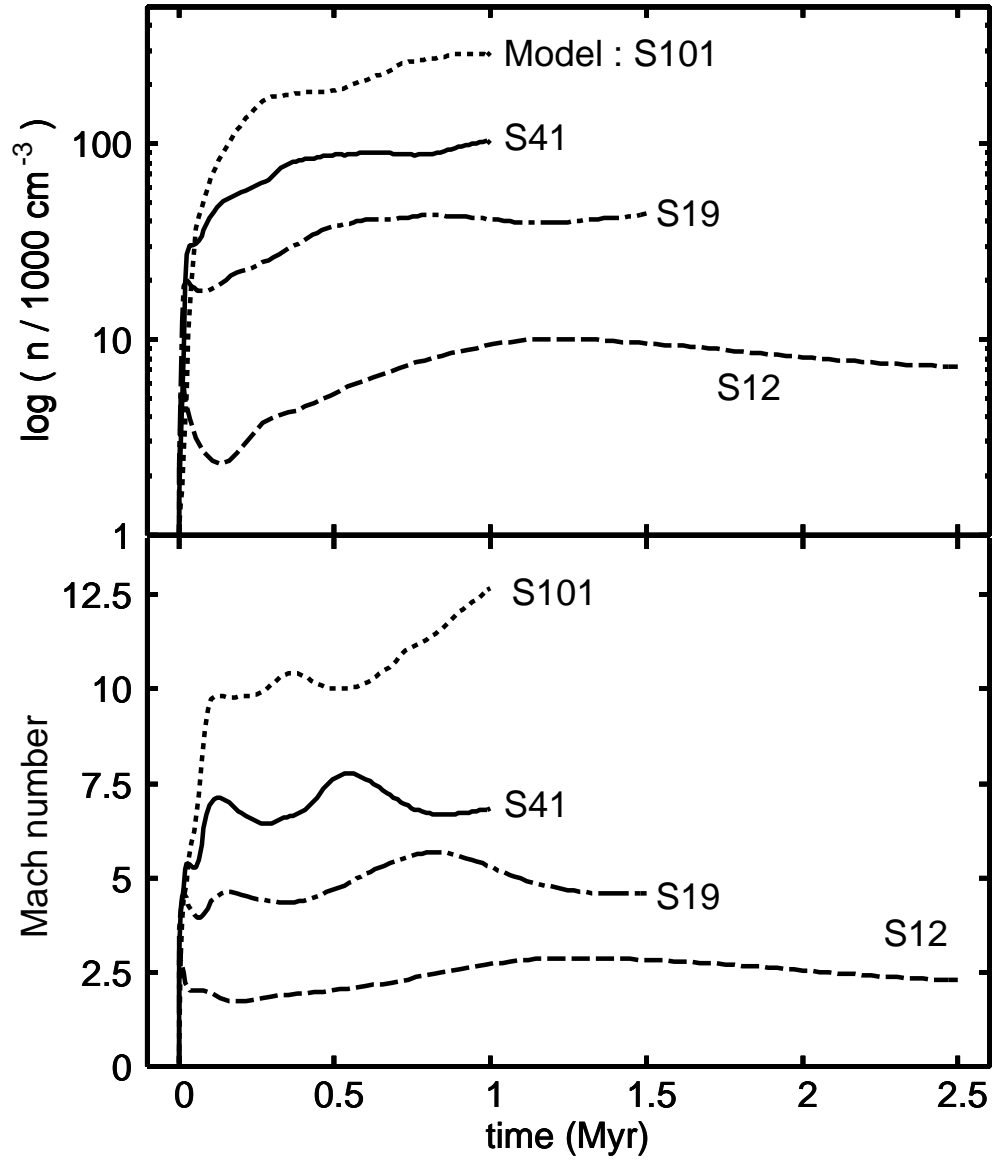


Fig. 17.— *Upper panel* : Time evolution of the maximum density of the shell in model S101 (dotted line), S41 (solid line), S19 (dot-solid line) and S12 (broken line). *Lower panel* : Time evolution of the Mach number of the SF in each model.